THE JOURNAL OF PHYSICAL CHEMISTRY C
A JOURNAL OF THE AMERICAN CHEMICAL SOCIETY

pubs.acs.org/JPCC

Article

Multifunctional Properties of FeMnScAl Quaternary Heusler Alloy: Insights into Spintronics, Photovoltaics, and Thermoelectric Applications

Hasan A. Masri, Mohammed S. Abu-Jafar,* Abdelmadjid Bouhemadou, and Nadjib Baadji

Cite This: *J. Phys. Chem. C* 2025, 129, 2672−2690

Read Online

ACCESS | Metrics & More | Article Recommendations

ABSTRACT: The increasing demand for efficient and low-cost multifunctional materials in the fields of spintronics, solar cell technology, and thermoelectric applications is a big challenge. The exceptional electronic and magnetic properties of Heusler alloys have made them promising candidates, allowing for fine-tuning for specific applications. This study investigates the elastic, structural, electronic, magnetic, optical, and thermoelectric properties of the FeMnScAl quaternary Heusler alloy using density functional theory with the full-potential linearized augmented plane wave method via Wien2K software and BoltzTraP for thermoelectric analysis. Results confirm that FeMnScAl is thermodynamically and mechanically stable, as evidenced by its negative formation energy and elastic constants meeting the stability criteria, with an optimized lattice parameter of 6.116 Å. Density of states and band structure analysis reveal its half-metallic character. The calculated magnetic moment of 3.00 μB follows the Slater-Pauling rule and stands for ferromagnetism. FeMnScAl also possesses special optical properties, such as a narrow band gap of 0.677 eV, a high refractive index ($2.63 < n(\omega) < 3.77$), low reflectivity in the visible region, strong UV absorption, and superluminal effects. This provides facilities for efficient light trapping and hence forms a candidate material to be used in photovoltaic applications. Finally, the thermoelectric properties reveal possible low-cost devices since FeMnScAl has shown a ZT value of 0.628 along with a high Seebeck coefficient of 196 μVK^{-1} at room temperature. With these results, it seems that FeMnScAl could be used in spintronic, thermoelectric, and green energy technologies. Further experiments are needed to confirm the efficacy of this material.

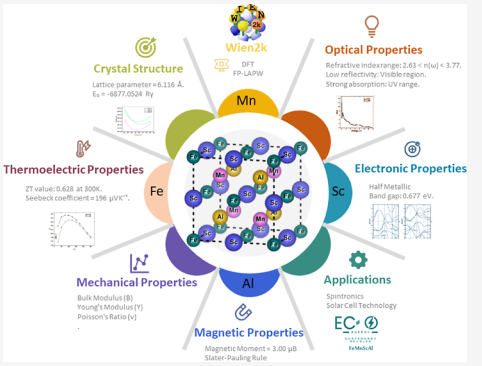

1. INTRODUCTION

The search for novel materials with special properties for green advanced technological applications has driven significant interest in Heusler alloys, a key class of materials in condensed matter physics and materials science. They are popular because their electronic and structural properties can be easily adjusted and customized. Their important magnetic features, strong light absorption, and high thermoelectric potential help in efficient energy conversion and open up possibilities for different smart systems like quantum computing, solar panels, temperature sensors, and control systems.[1−3] Heusler compounds are normally divided into two groups based on their chemical formula: full Heusler compounds and half Heusler compounds, with (formulas: X_2YZ and XYZ, respectively); X and Y are normally transition metals or rare earth metals, while Z is from the main group category in the periodic table.[4] Also, a new class of materials has come into prominence known as quaternary Heusler compounds. These have attracted considerable interest. Such a development further opens more ways for design improvement and enhancement of the properties. Such compounds are defined by the formulation (formula: XX′YZ), where X and X′ correspond to 3d or 4d transition metals, (Y) represents a rare earth element, and (Z) is a main group element.[5] The arrangement of atoms within the unit cell defines three distinct structural types distinguished by their Wyckoff position occupancy.[6]

Recent studies have shed light on the very promising potential of Heusler compounds. For instance, CoFeTiSn has been studied to show a half-metallic nature with remarkable spin polarization and thus stands as a good candidate for spintronic applications.[7] Similarly, CoFeXGe (X = Hf and Ta) and CrTiCoZ (Z = Al, Ga, and In) have shown potential in the application of spintronics and memory devices due to their high spin polarization and low Gilbert damping.[8,9] Although, LiHfPdZ (Z = Al, Ga, and In) and FeZrCrZ (Z = Si, Ge, and Sn), have been identified to be suitable for thermoelectric performance due to the high figures of merit ZT reported so

Received: September 29, 2024
Revised: January 10, 2025
Accepted: January 13, 2025
Published: January 22, 2025

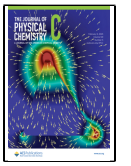

https://doi.org/10.1021/acs.jpcc.4c06553
J. Phys. Chem. C 2025, 129, 2672−2690

far, they prove that indeed efficient thermoelectric performance has been achieved.[10,11] AgCoFeZ (Z = Al, Ga, Si, Ge, and Sn), NiFeCrZ (Z = Al, Si, Ge, and In), and NdCoMnGa and CoFeXSn (X = Ru, Zr, Hf, and Ta) are also very promising for thermoelectric applications, since a record-high value of ZT has been possible with band engineering and nanostructuring.[12,13] First-principles calculations using CASTEP were performed for the electronic and magnetic properties of Heusler alloys FeMnScZ (where Z = Al, Ga, and In); it was found that FeMnScAl exhibits a remarkable 100% spin polarization at the Fermi level, hence, highlighting this compound as a potentially highly valuable material for spintronic applications. In addition, it has a total magnetic moment of 3 μB per unit cell, making it a potential candidate for magnetic applications. The thermodynamic stability and synthetic ability of this alloy are also confirmed by the Gao study.[14]

Many quaternary Heusler alloys (QHAs) remain less explored, which opens further opportunities for new materials discovery and unique properties. One such compound is the FeMnScAl alloy, which is rarely discussed in the literature, in particular, with regard to its possible applications in optics and thermoelectric fields. This work will provide a detailed study of the structural, electronic, magnetic, optical, and thermoelectric properties of FeMnScAl, and based on these findings present new insights into its multifunctionality for a wide range of applications.

The density functional theory (DFT) calculations are very helpful in studying the atomic properties of Heusler compounds,[15] and tools like Wien2K have proven to be complementary for this purpose.[16] The use of this computational method allows for efficient structure and electronic state predictions, making the system even more powerful in terms of predicting magnetic, electrical, as well as optical and thermoelectric behaviors.[17]

We dedicate the present work to the first comprehensive study of the properties and potential applications of the QHA FeMnScAl in modern technology using the latest Wien2K package. To date, no experimental data for the FeMnScAl compound have been reported in the literature. The study begins by probing the stability of the compound through systematic displacement of atomic positions along the main diagonal of the face-centered cubic lattice to identify the lowest-energy configuration. After that, the electronic, magnetic, optical, and thermodynamic properties are calculated.

A key novelty of this study is the discovery of FeMnScAl's unique optical and thermoelectric properties for next-generation technologies. This work significantly improves our understanding of FeMnScAl and provides a fundamental platform for further experimental investigations, material preparation, and applications in spintronics, photovoltaics, and thermoelectrics. Furthermore, the sophisticated methods used and the convincing outcomes presented constitute a reliable foundation for investigations of other promising QHAs. Such research efforts will contribute to designing new materials with tailored properties for emerging sustainable green technologies. The next section describes our computational methodology, followed by a section that gives our results in some detail. We then conclude the implications of these results, as well as make recommendations for further investigation of this exciting class of materials.

2. COMPUTATIONAL METHOD

The characteristics of the FeMnScAl quaternary Heusler compound were investigated using a computational methodology based on DFT.[15] Calculations in the current work were performed with the Wien2K package.[16] The method applied in the present work is the full-potential linearized augmented plane wave (FP-LAPW) approach, in which an augmented basis set is used to solve more precisely both electronic and structural properties.[18,19] We optimized crystal structures using the Perdew−Burke−Ernzerhof (PBE) exchange−correlation functional within the generalized gradient approximation (GGA);[20,21] to improve bandgap predictions, we employed the modified Becke-Johnson mBJ-GGA exchange-potential technique.[22−24] Our spin-polarized self-consistency calculations utilized a cubic structure in the 216 $F\bar{4}3m$ space group. Muffin-tin radii (RMT) of 2.38 a.u. for Fe and Mn and 2.32 a.u. for Sc and 2.20 for Al were chosen to avoid sphere overlap while maximizing enclosed volume. A plane wave cutoff of −8 Ry and a 165 special k-points IBZ (12 × 12 × 12 mesh, 2000 k-points in FBZ) was used. Structural optimization was achieved by minimizing the total energy and forces until convergence fell below 10^{-5} Ry/Bohr. This process involved relaxing the unit cell volume according to Murnaghan's equation of state, which subsequently allowed for the accurate calculation of structural parameters, including bulk modulus and lattice constant. The elastic constants were determined in the absence of pressure and zero Kelvin by calculating the total energy as a function of applied strain. For each elastic constant (C_{11} + $2C_{12}$, C_{11}−C_{12}, C_{44}) in the second-rank tensors, seven strain values ranging from −3 to +3% were applied. The energy-strain data were then fitted with a polynomial function, and the elastic constants were extracted from the second derivative of the energy with respect to strain by using of cubic-elastic package.[25,26] The optical matrix elements are calculated by the Wien2K optics package using the joint density of states (DOS).[27,28] In the spin-up state, FeMnScAl is metal, and after switching to setting 6 in the injoint, the plasma frequencies are identified in the FeMnScAl.outputjoint file. While in a spin-down state, the compound is found to be a semiconductor. To ensure accurate results, a denser k-point mesh of 10,000 and Drude contributions must be defined. Then, a Kramers−Kronig transformation is applied to obtain the optical characteristics.[29] Lastly, to accurately compute thermoelectric transport properties, a denser k-point mesh (10,000 k-points) was generated, and the corresponding eigenvalues for both spin-up and spin-down states were calculated. Using these eigenvalues (after obtaining the Fermi energy and electron number), BoltzTraP was then employed to determine the transport properties.[30]

3. RESULTS AND DISCUSSION

3.1. Structural Properties and Thermodynamic Stability. The FeMnScAl compound has a face-centered cubic structure and crystallizes in the Fm-43 space group of number 216, following the LiMgPdSn-type structure. Due to the symmetry considerations of the cubic structure, three possible types were examined according to their atomic occupancy positions in order to select the most stable type refine. When the Al main group atom is placed at the 4d site (0.75, 0.75, and 0.75), there are three possible arrangements for Fe, Mn, and Sc atoms among the 4a (0, 0, 0), 4c (0.25, 0.25, 0.25), and 4b (0.5, 0.5, 0.5) (see Table 1).[6,31,32] These

https://doi.org/10.1021/acs.jpcc.4c06553
J. Phys. Chem. C 2025, 129, 2672−2690

Table 1. Atomic Arrangements Calculated Structural Properties and Formation Energy of FeMnScAl Compound

	atom/property	type 1	type 2	type 3
atomic positions	Fe	(0,0,0)	(0,0,0)	(1/4,1/4,1/4)
	Mn	(1/4,1/4,1/4)	(1/2,1/2,1/2)	(0,0,0)
	Sc	(1/2,1/2,1/2)	(1/4,1/4,1/4)	(1/2,1/2,1/2)
	Al	(3/4,3/4,3/4)	(3/4,3/4,3/4)	(3/4,3/4,3/4)
structural properties	a (Å)	6.1532	6.1142 6.2[14]	6.215
	E0 (Ry)	−6877.00151	−6877.0524	−6877.01941
	B (GPa)	106.6302	119.5695	96.3299
	B'	5.5122	5.0653	4.2207
	EForm (Ry)	−0.681635	−0.732528	−0.699536

structural configurations were examined using a volume optimization approach that was based on the Murnaghan equation of state, which offers a theoretical framework to model the total energy and pressure as a function of the volume per formula unit. This relationship is mathematically represented by eq 1[33]

$$E(V) = E_0(V) + \frac{BV}{B'}\left[\frac{\left(\frac{V_0}{V}\right)^{B'}}{B'-1} + 1\right] - \frac{BV_0}{B'-1} \quad (1)$$

The parameters consist of E_0, the minimum energy; B, the bulk modulus; B', the pressure derivative of the bulk modulus, which represents the change in bulk modulus under pressure; and V_0, the equilibrium volume. These values are fundamental for this analysis.[34] The bulk modulus B is related to the pressure P and volume V through the differentiation formulas $B = -V\frac{dP}{dV} = V\frac{d^2E}{dV^2}$, where $P = -\frac{dE}{dV}$.

Figure 1 presents the optimized energy values as a function of volume for the six atomic arrangements of FeMnScAl. By

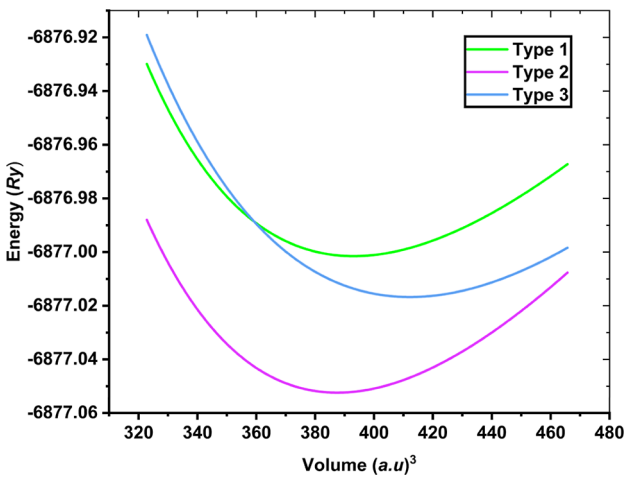

Figure 1. Variation of total energy with unit cell volume for three different FeMnCrAl types.

comparing the energy values for these atomic arrangements, it can be said that FeMnScAl type 2: Fe at 4a (0, 0, 0), Mn at 4b (0.5, 0.5, 0.5), Sc at 4c (0.25, 0.25, 0.25), and Al at 4d (0.75, 0.75, 0.75) has the most stable atomic arrangement, since its energy is the lowest at zero pressure and absolute zero temperature compared to the remaining two atomic arrangements.

Table 1 provides a summary of the key equilibrium structural parameters, which include optimized energy (E_0), lattice parameter (a_0), bulk modulus (B), and its derivative (B').

Figure 2 illustrates the crystalline arrangement of the FeMnScAl compound, depicting three distinct types of structures alongside the associated Brillouin zone, which include high-symmetry points and reciprocal vectors.

The thermodynamic stability of the FeMnScAl compound can be gauged by its formation energy (E_{Form}).[35,36] This energy is absorbed or released when a compound is formed from its elements under standard conditions.[37] Equation 2 was employed to calculate the formation energy (E_{Form}) of the three types of FeMnScAl QHA[38]

$$E_{Form} = E^{Cubic}_{FeMnScAl(x)} - (E^{Cubic}_{Fe} + E^{Cubic}_{Mn} + E^{Cubic}_{Sc} + E^{Cubic}_{Al}) \quad (2)$$

where $E^{Cubic}_{FeMnScAl(x)}$ is the lowest energy of the compound and E^{Cubic}_{Fe}, E^{Cubic}_{Mn}, E^{Cubic}_{Sc}, and E^{Cubic}_{Al} are the minimum energies of Fe, Mn, Sc, and Al, respectively (x = 1, 2, and 3), is the type number. The negative formation energy of FeMnScAl at zero Kelvin and zero pressure calculated in Table 1 suggests that the elements could combine and form the alloy.

To assess the dynamic stability of the studied compound, we calculated its phonon dispersion curve. This study used the linear response method as implemented in the CASTEP code.[39] Figure 3 illustrates the resulting phonon dispersion diagram for the considered material. Theoretically, a material is considered dynamically stable when its phonon dispersion spectrum does not contain soft modes (also called imaginary modes, characterized by negative frequencies) and dynamically unstable when it does. These soft modes trigger lattice instability, leading to structural phase transitions. Moreover, their presence may indicate that the synthesis of the compound under the standard conditions might be complex. Figure 3 shows that the compound FeMnScAl exhibits no soft modes, indicating that it is dynamically stable.[40−44]

3.2. Charge Density and Bond Analysis. Chemical bonding can be effectively represented using charge density, which describes the interaction range between atoms based on electron cloud distribution. This method is widely applied in the study of charge distribution. In Figure 4a,b, the 2D charge density contours of the FeMnScAl alloy are shown in the (110) plane for both majority and minority spins. The spherical symmetry observed in the charge distribution around Fe and Mn atoms points to ionic bonding.[45,46] Conversely, the distortion and elongation of the charge density contours around Sc and Al, directed toward neighboring atoms, suggest covalent interactions with these neighbors.[47] The differences in electronegativity among the constituent elements Fe (1.83),

https://doi.org/10.1021/acs.jpcc.4c06553
J. Phys. Chem. C 2025, 129, 2672−2690

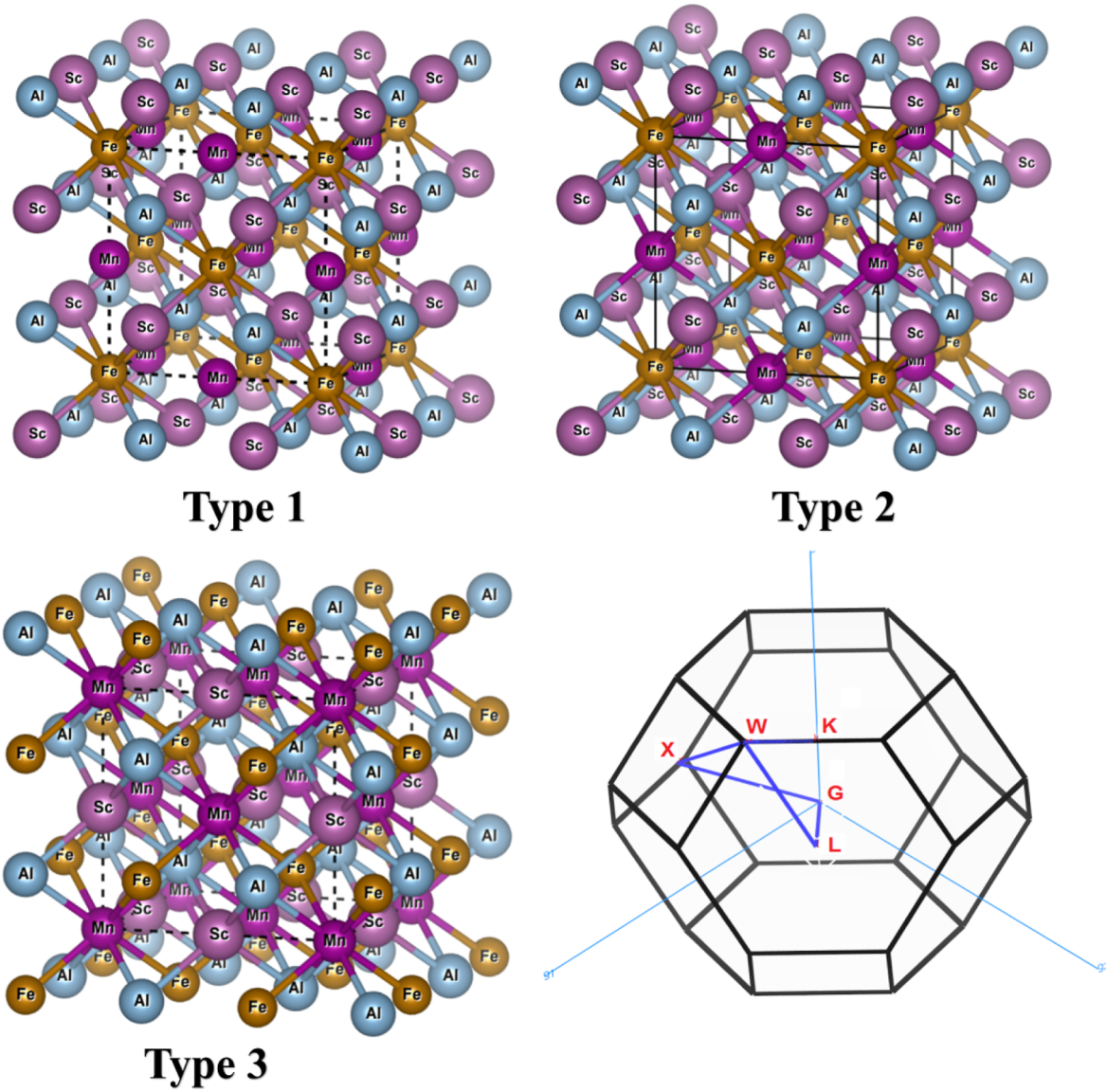

Figure 2. Three crystal structures of FeMnScAl and its Brillouin zone with high-symmetry points.

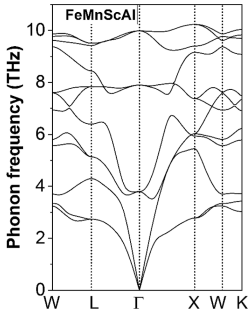

Figure 3. Phonon dispersion curve of FeMnScAl along the high-symmetry directions in the Brillouin zone.

Mn (1.55), Sc (1.36), and Al (1.61) likely account for this variation in the bond nature.

3.3. Elastic Properties. The resistance of a material to deformation is reflected in its elastic properties, which are of fundamental importance when considering most industrial applications. This section inspects the mechanical stability of QHA FeMnScAl by calculating its elastic constants (C_{ij}) and related properties under conditions of zero pressure and temperature at absolute zero. The Reuss approximation method was employed to determine the anisotropic factor (A), Poisson's ratio (ν), shear modulus (S_R), bulk modulus (B), and Young's modulus (Y) for QHA FeMnScAl through the following equations[48]

$$S_R = \frac{5C_{44}(C_{11} - C_{12})}{4C_{44} + 3(C_{11} - C_{12})} \tag{3}$$

$$B = (C_{11} + 2C_{12}) \tag{4}$$

$$\nu = \frac{3BS - 2S_R}{2(3B + S_R)} \tag{5}$$

$$A = \frac{2C_{44}}{(C_{11} - C_{12})} \tag{6}$$

$$Y = \frac{9BS_R}{(S_R + 3B)} \tag{7}$$

https://doi.org/10.1021/acs.jpcc.4c06553
J. Phys. Chem. C 2025, 129, 2672−2690

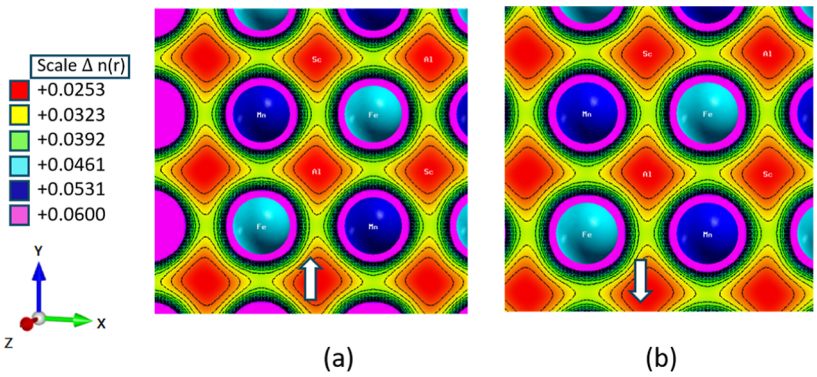

Figure 4. (a,b) Charge density contours of the FeMnScAl alloy.

Table 2. Elastic Constants of the QHA FeCrScAl at Zero Strain ($\delta = 0$)[a]

type	C_{11}	C_{12}	C_{44}	S_R	B	B/S_R	Y	v	A
1	111.573	102.778	93.508	10.269	105.71	10.294089	29.840	0.452	21.26390
2	154.9892	103.6927	75.6698	42.508	120.791	2.8416063	114.135	0.342	2.950291
3	85.624	69.996	79.593	17.027	75.205	4.4168086	47.496	0.394	10.18594

[a]Note: The values for C_{11}, C_{12}, C_{44}, S_R, Y, and B are expressed in Giga-Pascals (GPa).

To achieve conventional mechanical stability, the material's elastic constants must meet these requirements: $C_{11} > 0$, $C_{11} + 2C_{12} > 0$, $C_{12} < B < C_{11}$, $C_{11}-C_{12} > 0$, and $C_{44} > 0$, the findings indicate that FeMnScAl is mechanically stable.[49] Table 2 presents the calculated mechanical properties of FeMnScAl at zero strain, zero pressure, and zero absolute temperature.

The mechanical stability and chemical bonds of QHA FeMnScAl were analyzed in this study. The calculated shear and bulk moduli highlight the material's resistance to deformation under stress.[50] The calculated shear modulus S_R and bulk modulus B highlight the material's resistance to deformation under stresses.[50] A high Young's modulus indicates stiffness in materials, whereas a low Young's modulus suggests flexibility.[51] Poisson's ratio provides insight into a material's response to stress, stability, and bonding properties. If Poisson's ratio is greater than 0.26, then the material is classified as ductile; otherwise, it is classified as brittle. The calculated Poisson's ratios of the three types are higher than the critical threshold of 0.26, which points to the ductileness of FeMnScAl.[52,53] The B/S_R values of FeMnScAl tell us that the material is ductile since the values are much beyond the brittleness threshold of 1.75.[51] Poisson's ratio values can also be used to distinguish between ionic and covalent bonds, with values below 0.25 suggesting ionic bonds and those above 0.25 indicating covalent bonds. The computed Poisson's ratios of the three types suggest the presence of covalent bonding.[54] It is also noticed that the value of the anisotropic factor (A) is other than unity, which indicates that the mechanical properties of FeMnScAl are direction-dependent, hence anisotropic in nature.[50,55] These observations are of high significance in understanding the behavior of the material for industrial applications.

Electronic, optical, and thermoelectric analyses and results are restricted to the type 2 structure. This structure has been determined to be thermodynamically and mechanically stable as well as have the lowest energy configuration.

3.4. Electronic Properties. The importance of electronic properties is based on the understanding of chemical bonds between the elements and their alloys; this gives a clear picture of basic interactions between elements. The DOS and band structure of the FeMnScAl alloy type 2 will be analyzed. The analysis of the calculated total and partial DOS using the GGA and mBJ approximations to understand the energy band gap origin is presented in Figures 5a–e and 6a–e. Under the two methods of approximation, the DOS near the Fermi level mainly comes from the d-orbitals of Fe, Cr, and Sc for both the conduction and valence bands. A small contribution can also be noted from the p- and s-orbitals of these elements in both spins' channels. The compound displays a half-metallic characteristic with 100% spin polarization, arising from the presence of spin-up states and the absence of spin-down states at the Fermi level, suggesting potential applications in spintronic devices.

The electronic band structure calculation results of the spin-up and spin-down states of the FeMnScAl alloy using GGA and mBJ are depicted in Figure 7a–d. The results reveal metallic behavior in the majority spin channel with bands crossing the Fermi level. The minority spin channel shows semiconducting properties with an indirect bandgap. The magnitude of this gap varies depending on the computational method: 0.14562 eV for GGA and 0.1574 eV for mBJ. This difference arises from how each method treats the exchange–correlation potential. GGA incorporates the electron density gradient; however, it frequently underestimates the exchange–correlation potential where rapid density changes occur, which leads to reduced band gap values. In contrast, mBJ employs a semilocal approach incorporating density and kinetic energy density, providing a more precise approximation of the exchange–correlation effects near the Fermi level. As a result, the mBJ method yields more precise band gap calculations, consistently matching experimental measurements and enhancing our understanding of electronic characteristics.[24] Band gap results from mBJ frequently match experimental values more closely than those from GGA, making it an essential tool for material prediction and screening.[22] In the first Brillouin zone, the valence band reaches its maximum at X, while the conduction band attains its minimum at L. These characteristics provide evidence for the half-metallic nature of the FeMnScAl alloy.

https://doi.org/10.1021/acs.jpcc.4c06553
J. Phys. Chem. C 2025, 129, 2672–2690

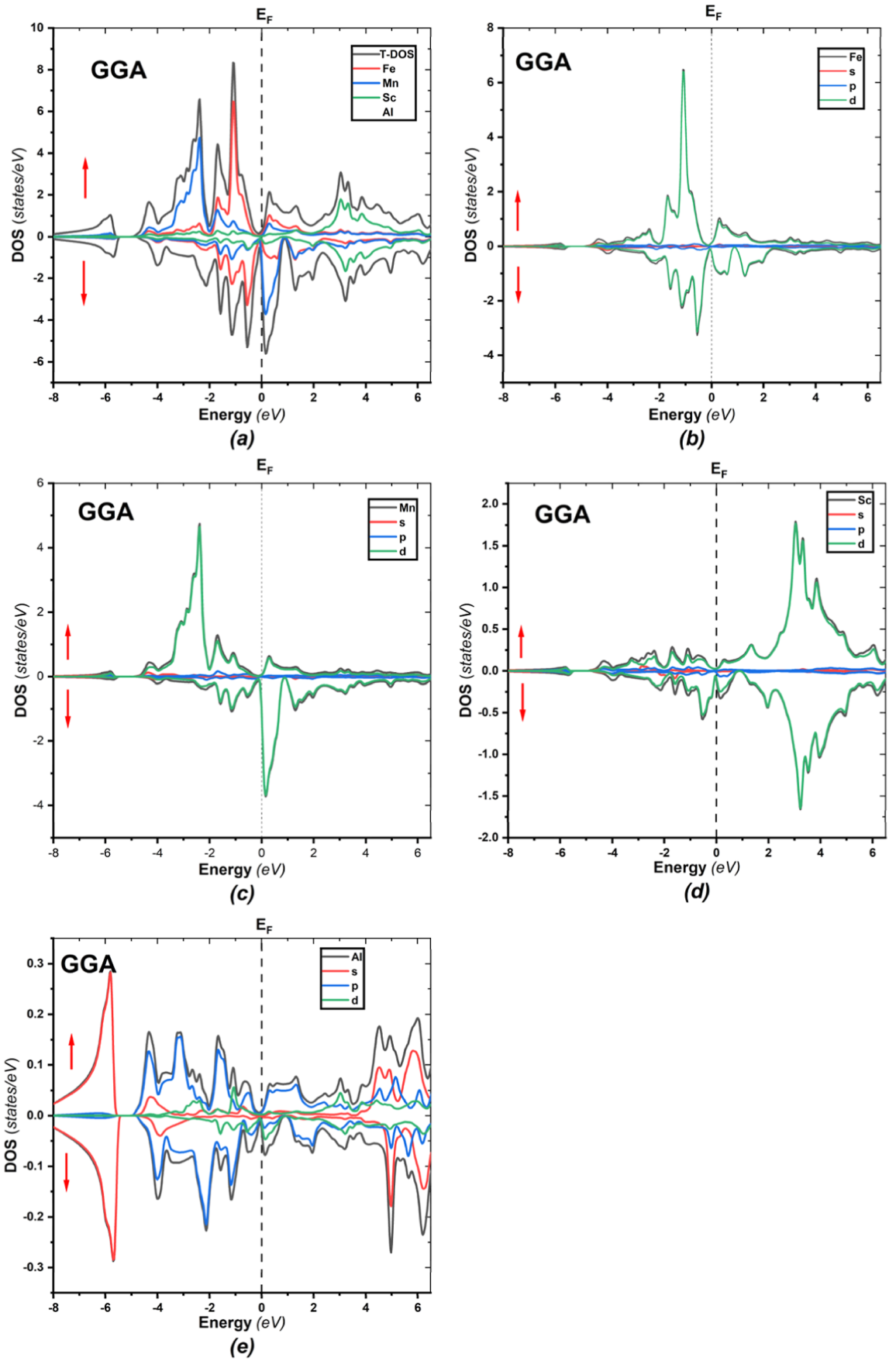

Figure 5. (a–e) Total and atomic contributions to the DOS of FeMnScAl using the GGA.

https://doi.org/10.1021/acs.jpcc.4c06553
J. Phys. Chem. C 2025, 129, 2672–2690

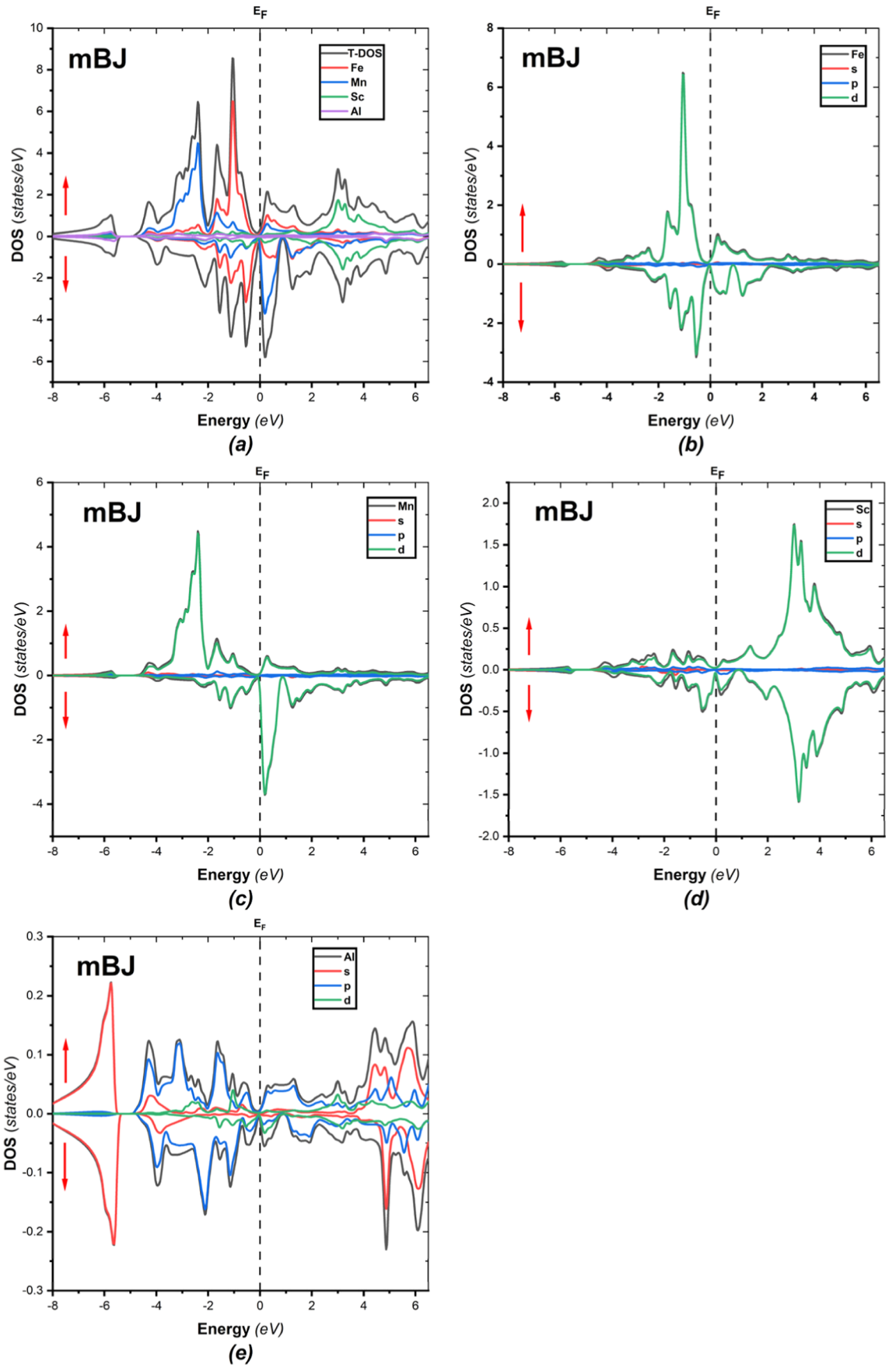

Figure 6. (a–e) Total and atomic contributions to the DOS of FeMnScAl using the mBJ approximation.

https://doi.org/10.1021/acs.jpcc.4c06553
J. Phys. Chem. C 2025, 129, 2672−2690

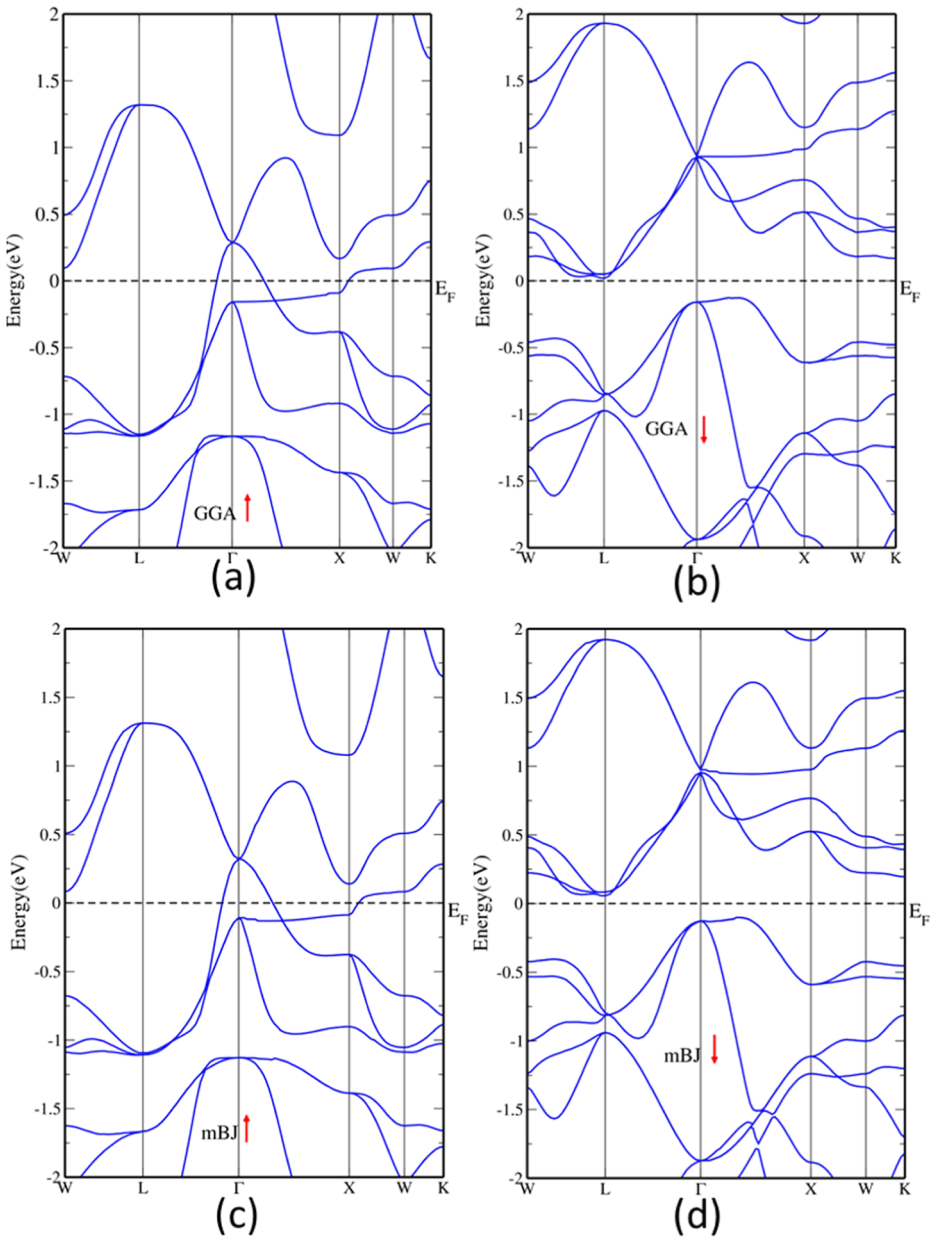

Figure 7. (a–d) Spin-polarized electronic band structures of the FeMnScAl alloy calculated using GGA and mBJ.

Table 3. Calculated Total and Partial Magnetic Moments (μ) for FeMnScAl in (μB) Using GGA and mBJ Methods

type	exchange potential	interstitial	μ_{Fe}	μ_{Mn}	μ_{Sc}	μ_{Al}	μ_{Tot}
1	GGA	0.00845	0.55277	2.52363	−0.04105	−0.04392	2.99987
	mBJ	−0.19137	0.63505	2.71301	−0.09468	−0.06201	3.0000
2	GGA	−0.07580	0.42708	2.85759	−0.15056	−0.05880	2.99951
	mBJ	−0.03687	0.02084	3.15503	−0.09040	−0.04886	2.99973
3	GGA	−0.22531	1.83863	2.85152	−0.25582	−0.09485	4.11416
	mBJ	−0.35102	1.95022	3.05055	−0.31804	−0.12842	4.20329

3.5. Magnetic Properties. The magnetic properties of a material can be described by its total magnetic moment. For the FeMnScAl alloy, the interstitial, total, and partial magnetic moments were calculated using the GGA and mBJ methods (see Table 3). This type 2 FeMnScAl alloy obeys the Slater-Pauling behavior, given by $M_{tot} = Z_{tot} - 24$. Here, M_{tot} is the total magnetic moment per formula unit, whereas Z_{tot} is the total number of valence electrons. The electronic valence configurations of Fe, Mn, Sc, and Al have the expressions Fe $3d^6 4s^2$, Mn $3d^5 4s^2$, SC $3d^1 4s^2$, and Al $3s^2 3p^1$. The Slater-Pauling predicts a total magnetic moment of 3 μB for its 21 valence electrons; this prediction aligns well with the calculated magnetic moments in the alloy FeMnScAl for types 1 and 2. The magnetic moment distribution shows large positive contributions from Mn atoms, substantial negative moments from Cr atoms, smaller positive moments from Fe atoms, and

https://doi.org/10.1021/acs.jpcc.4c06553
J. Phys. Chem. C 2025, 129, 2672−2690

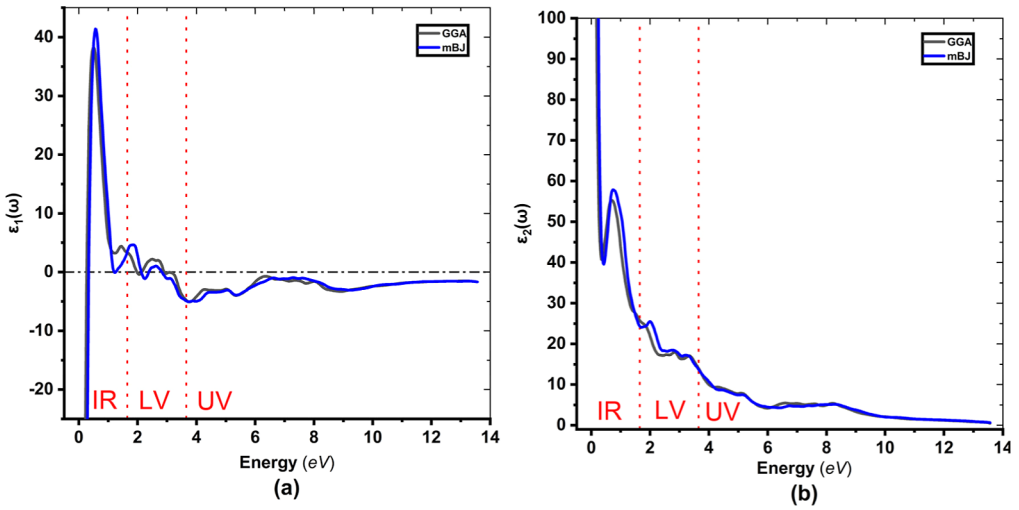

Figure 8. (a,b) Dielectric function of FeMnScAl using mBJ and GGA methods.

negligible positive moments from Ge atoms. The results are revealing in that the FeMnScAl alloy has a total magnetic moment of 3.00 μB, representing that this alloy is a perfect half-metallic material. In addition, the total magnetic moment of type 3 is noninteger. The result obtained in this study is in perfect agreement with the findings of Y. C. Gao and X. Gao on the magnetic properties of the FeMnScAl alloy.[14] Optical and thermoelectric analyses and results will be restricted to the type 2 structure. This structure has been determined to be thermodynamically and mechanically stable and exhibits the most pronounced half-metallic band gap.

The magneto-crystalline anisotropy (MCA) of FeMnScAl was evaluated through calculations performed using the FLEUR code,[56] where spin−orbit coupling (SOC) was introduced in the muffin-tin spheres through the second-variation technique.[18,57] Defined as the total energy difference between the [110] and [001] magnetization directions, the MCA was found to be 0.96 meV per formula unit. To ensure accuracy, convergence testing was rigorously performed, especially for the Brillouin zone sampling. Stable magnetization under thermal agitation requires the sample volume (V) and MCA to satisfy the stability criterion, $K_vV > 60\ k_BT$, where K is the volume MCA, k_B is the Boltzmann constant, and T is the absolute temperature.[58] Nearest-neighbor exchange coupling was strong about 30 meV, leading to an estimated Curie temperature (T_c) of approximately 1200 K by using a mean-field approximation. This estimation likely overstates T_c as it neglects spin-wave excitations and long−range correlations. Accurate calculations, requiring spin-spiral methods and mapping to a Heisenberg model are computationally demanding.

3.6. Optical Properties. Understanding the optical properties of the FeMnScAl compound is very important in order to know its potential applications in practical fields such as optoelectronics, solar energy, and photonics. The response of the compound to external electromagnetic waves in the spectral range extending from infrared (IR) to ultraviolet (UV) [0−14 eV] is examined by employing two approximate methods, namely, GGA and mBJ. The study of the dielectric function, optical conductivity, reflectivity, excitation coefficient, absorption coefficient, and energy loss of the electron as a function of photon energy is shown in Figures 8−13. The dielectric function $\varepsilon(\omega)$ is considered the cornerstone for understanding the optical properties of the compound. Through this function, all optical characteristics of the material can be calculated. The dielectric function is computed using eq 8[59−61]

$$\varepsilon(\omega) = \varepsilon_1(\omega) + i\varepsilon_2(\omega) \tag{8}$$

The real part $\varepsilon_1(\omega)$ is directly calculated using the Kramers−Kronig relation[62]

$$\varepsilon_1(\omega) = \mathrm{Re}\varepsilon_{ij}(\omega) = \sigma_{ij}\frac{2}{\pi}p\int_0^\infty \frac{\acute{\omega}\mathrm{Im}\ \varepsilon_{ij}(\omega)}{\hat{w}^2 - \omega^2} \tag{9}$$

While the imaginary part of the dielectric function $\varepsilon_2(\omega)$ is given by

$$\varepsilon_2(\omega) = \mathrm{Im}\ \varepsilon_{ij}(\omega)\frac{h^2e^2}{\pi m_e^2\omega^2}\sum\int \mathrm{d}k\Psi_k^{cn}|\mathbf{p}^i|\Psi_k^{vn}\Psi_k^{vn}|\mathbf{p}^\beta|\Psi_k^{cn}$$
$$\sigma(E_k^{cn} - E_k^{n\nu} - \omega) \tag{10}$$

Equation 10 describes electronic transitions between occupied valence band (vn) states, $|\Psi_k^{vn}>$ with energy E_k^{vn}, and unoccupied conduction band (cn) states, $|\Psi_k^{on}>$ with energy E_k^{on}, and P is the momentum operator. Since FeMnScAl is a half-metallic alloy, its dielectric function characterized by two contributions $[\varepsilon(\omega) = \varepsilon_{[\mathrm{intra}]}(\omega) + \varepsilon_{[\mathrm{inter}]}(\omega)]$. Intraband transitions, where electrons move to higher energy levels within the same band, and interband transitions, where electrons shift from one energy band to another when the material absorbs electromagnetic radiation. This phenomenon is known as the bound electron effect.[63]

The dielectric function of FeMnScAl, as depicted in Figure 8, is examined across a broad wavelength range extending from the IR and visible light (LV) to the UV. The real part of the dielectric function $\varepsilon_1(\omega)$ exhibits metallic behavior at low energies due to negative values for both approximations, as shown in Figure 8a.[64] These negative values extend from negative infinity to the first plasma frequency $[\varepsilon_1(\omega) = 0]$, which is ∼0.28 eV for both GGA and mBJ. Several plasma frequencies are observed at ∼1.97, 2.16, and 2.89 eV for GGA and 2.05, 2.35, and 2.76 eV for mBJ.[65] Positive $\varepsilon_1(\omega)$ values indicate dielectric behavior, allowing electromagnetic waves to propagate. This strong positive response is observed in two distinct regions: the IR, from 0.28 to 1.65 eV, and the LV

https://doi.org/10.1021/acs.jpcc.4c06553
J. Phys. Chem. C 2025, 129, 2672−2690

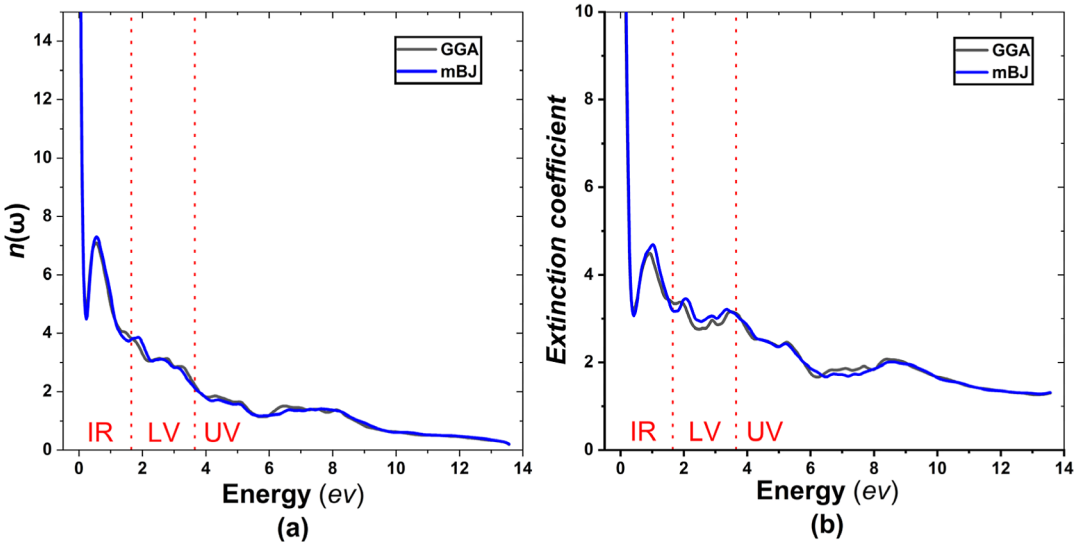

Figure 9. (a) Energy dependence of refractive index and (b) extinction coefficient in FeMnScAl by using mBJ and GGA methods.

range, from 1.65 to 1.97 eV, for GGA and from 0.28 to 1.129 eV mBJ approaches. The highest peak appears at 0.5034 eV for GGA and mBJ, and other smaller peaks appear in the LV region. These peaks happen when the material absorbs photons whose energy matches the difference between electron energy levels,[60] indicating that this alloy has a great response for IR and LV spectra. $\varepsilon_1(\omega)$ becomes trivial above ∼9 eV.

Figure 8b shows the imaginary part of the dielectric function, revealing the material's metallic behavior. Both approximation methods (GGA-mBJ) show high positive $\varepsilon_2(\omega)$ values at low energies, and then the curves drop sharply until around 0.0.23 eV. After this point, the curves start to increase, reaching their maximum at 0.61 eV for both (GGA-mBJ) within the IR light range. This peak represents electron transitions between valence and conduction bands. With increasing photon energy, $\varepsilon_2(\omega)$ in both curves shows a gradual decrease, with small variations, eventually nearing zero at energies of ∼10 eV and beyond.

The complex refractive index, $n(\omega)$, is an important parameter in characterizing the optical properties of a material. It consists of the refractive index $\eta(\omega)$, which governs light propagation, and the extinction coefficient $\kappa(\omega)$, which quantifies light absorption. This relationship is mathematically represented by eq 11[66]

$$n(\omega) = \eta(\omega) + i\kappa(\omega) \tag{11}$$

The refractive index $n(\omega)$ and extinction coefficient $\kappa(\omega)$ for the GGA and mBJ approaches are represented in Figure 9 as functions of photon energy. Figure 9a reveals that the curves of both $n(\omega)$ and $\kappa(\omega)$ start from infinity at low energies, suggesting the presence of free electrons and FeMnScAl's metallic characteristics.[64] One peak appears in the near-IR spectrum at ∼0.6 eV; this is a result of interband transitions. When the photon energy exceeds 8 eV, the refractive index $n(\omega)$ falls below 1, which corresponds to negative $\varepsilon_1(\omega)$ values. This subunity refractive index $n(\omega)$ implies potential superluminal effects, which could be useful in optical applications.[67,68] A significant refractive index is noted in the visible range, where values are observed to be between 2.63 and 3.77. Figure 9b demonstrates a general decline in the extinction coefficient as photon energy increases, and in the range of $(2.69 < \kappa(\omega) < 3.35)$ in the visible spectrum.

The absorption coefficient measures how the material absorbs light of specific energies per unit thickness. This absorption happens when light interacts with the material's electrons, causing them to shift between energy levels; this is given by eq 12[69−71]

$$\mathrm{A}(\omega) = \frac{2\omega\kappa(\omega)}{c} \tag{12}$$

where $\kappa(\omega)$ is the extinction coefficient and (c) is the speed of light in vacuum. Figure 10 illustrates the absorption coefficient

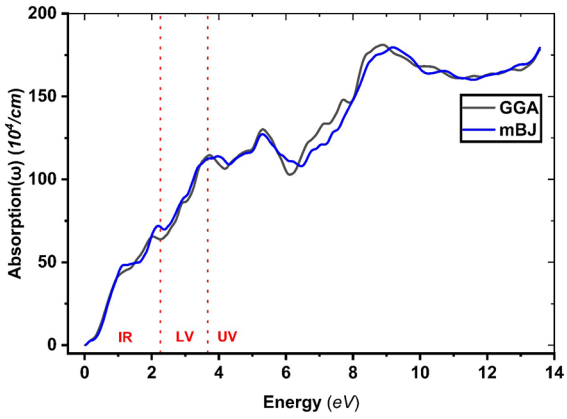

Figure 10. Absorption coefficient A(ω) spectrum of the FeMnScAl alloy (mBJ and GGA).

variations with the photon energy used by the GGA and mBJ methods. From these results, it is indicated that the FeMnScAl alloy absorbs low energy light due to its metallic nature. However, as photon energy rises, so does the absorption coefficient, For the mBJ, the absorption peaks were observed at 3.9, 5.26, and 9.18 eV in the UV, while the GGA method shows peaks at 3.70, 5.31, and 8.87 eV in the UV. This shows that with higher energy levels of incoming radiation, the material begins to absorb more energy at specific energy levels.[72] The low extinction coefficient in the UV region results from the high absorbance of the FeMnScAl compound in that area.[73,74] Furthermore, materials that have both narrow bandgaps and significant UV light absorption are found to be

https://doi.org/10.1021/acs.jpcc.4c06553
J. Phys. Chem. C 2025, 129, 2672−2690

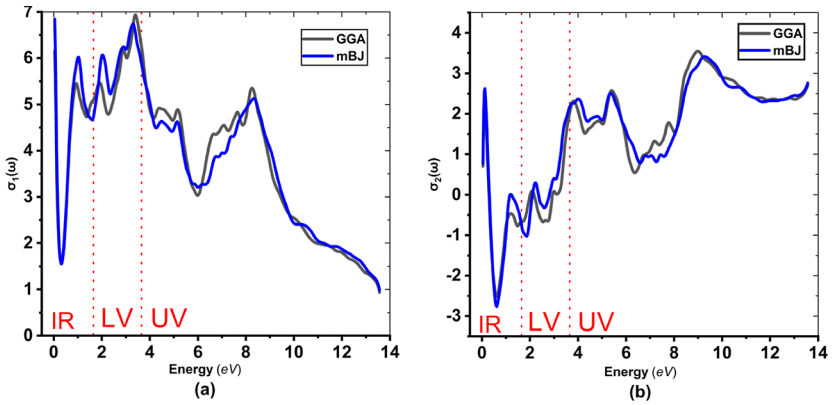

Figure 11. (a,b) Optical conductivity $\sigma(\omega)$ spectrum of the FeMnScAl alloy (mBJ and GGA).

appropriate for use in optoelectronic devices and solar cells.[75,76] These findings emphasize that the FeMnScAl alloy has significant absorption in the UV range, supporting its potential for optoelectronic applications.

The optical conductivity $\sigma_1(\omega)$ consists of two components: the real part (ω) and the imaginary part $\sigma_2(\omega)$, as shown in eq 13[77]

$$\sigma(\omega) = \sigma_1(\omega) + i\sigma_2(\omega) = -i\varepsilon_0\omega(\varepsilon(\omega) - 1) \tag{13}$$

The optical conductivity spectra $\sigma_1(\omega)$, as a function of light energy, are presented in Figure 11a, which shows the real part of the conductivity spectrum. Both GGA and mBJ show multiple peaks as the energy increases. The highest peaks appear around 2−6 eV, this suggests that absorbing radiation produces more free charge carriers.[78] The absorption coefficient data align with this observation. As the energy surpasses 6 eV, the conductivity starts to decline, with both methods converging toward lower values as the energy reaches approximately 12 eV. Figure 11b shows the imaginary part of the conductivity $\sigma_2(\omega)$. The graph shows differences in peak intensities and positions for GGA and mBJ, even though they follow similar trends. The phase shift depends on the imaginary conductivity. Electrons are resistive at low frequencies ($\sigma_2 < \sigma_1$) but become inductive in the UV ($\sigma_2 > \sigma_1$), storing energy and delaying response to the external electric field.[79] Inductive behavior is used in industrial heating applications.[34]

The reflectivity $R_{ij}(\omega)$ represents the fraction of incident electromagnetic radiation reflected by a material at a given frequency. It is determined by the dielectric function $\varepsilon(\omega)$, which is obtained in terms of $\mathrm{Re}\varepsilon_{ij}$ and $\mathrm{Im}\varepsilon_{ij}$ by the given relationship[80]

$$R_{ij}(\omega) = \left[\frac{(\mathrm{Re}\varepsilon_{ij} + i\mathrm{Im}\varepsilon_{ij})^2 - 1}{(\mathrm{Re}\varepsilon_{ij} + i\mathrm{Im}\varepsilon_{ij})^2 + 1}\right] \tag{14}$$

Figure 12 shows the optical reflectivity $R_{ij}(\omega)$ of FeMnScAl as a function of energy using the mBJ and GGA methods. Reflectivity starts high near 0 eV, decreases to a minimum around ∼6.45 − ∼7.9 eV of 0.34 (that mean 66% of the incident light transmitted within this compound at this range), and then rises again toward 14 eV. Both methods display similar trends.

$L_{ij}(\omega)$, which indicates the energy loss experienced by electrons due to an electromagnetic wave, is related to plasmon excitations and electronic transitions in the material

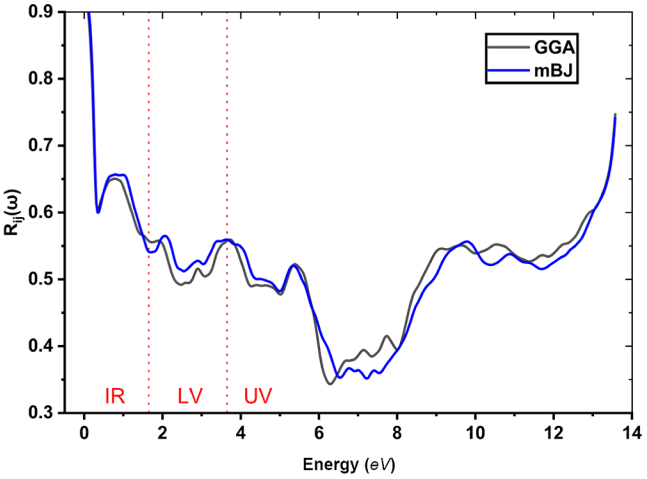

Figure 12. Optical reflectivity R(ω) spectrum of the FeMnScAl alloy (mBJ and GGA).

$$L_{ij}(\omega) = -\mathrm{Im}\left\{\frac{1}{\varepsilon_{ij}(\omega)}\right\} = \frac{\mathrm{Im}\,\varepsilon_{ij}}{(\mathrm{Re}\varepsilon_{ij})^2 + (\mathrm{Im}_{ij})^2} \tag{15}$$

The energy loss function $L_{ij}(\omega)$ of FeMnScAl, as obtained from both mBJ and GGA, as illustrated in Figure 13, shows similar general features but with small differences in peak position and intensity. Both schemes display a gradual rise in

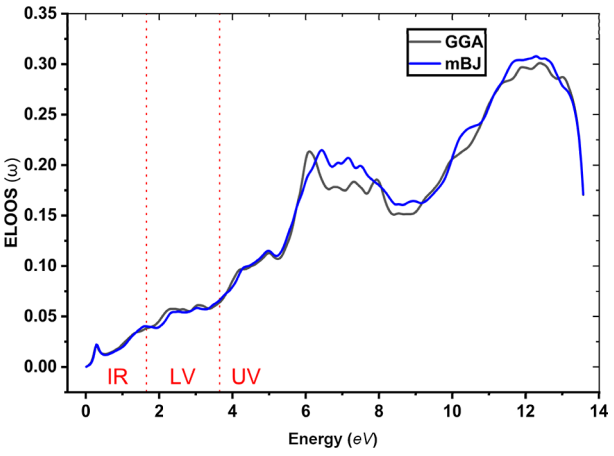

Figure 13. Energy loss function $L(\omega)$ spectrum of the FeMnScAl alloy (mBJ and GGA).

https://doi.org/10.1021/acs.jpcc.4c06553
J. Phys. Chem. C 2025, 129, 2672−2690

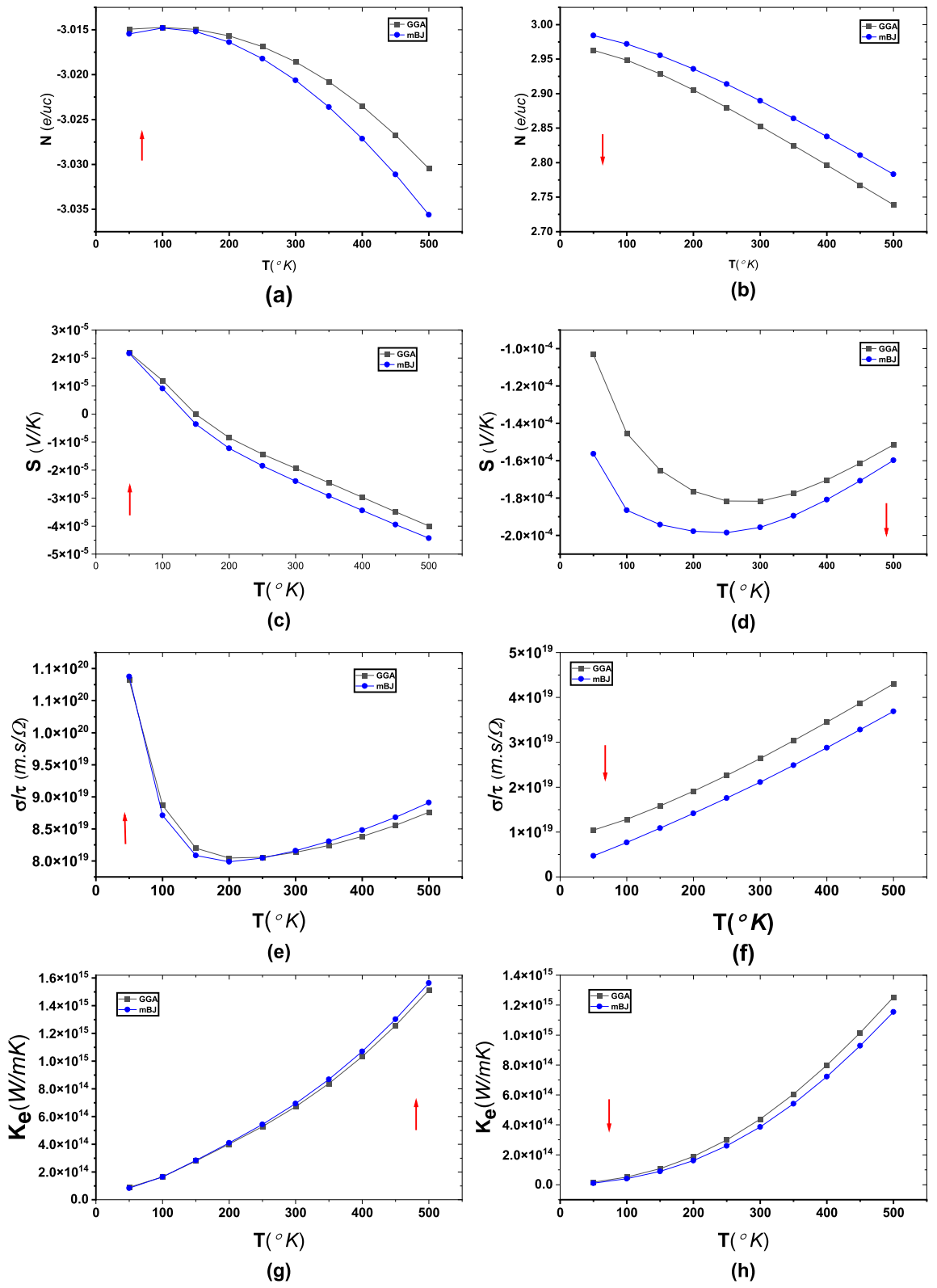

Figure 14. Thermoelectric properties of the FeMnScAl compound.

energy loss from 0 to 5 eV, reaching a strong peak around 6 eV in which the GGA curve has a slightly sharper peak compared to the mBJ one. Indeed, the mBJ approach does predict slightly higher energy loss values around the second peak at 12 eV. These differences may be because mBJ treats some electronic interactions more strongly than GGA.[20]

Our findings show that the special optical features of FeMnScAl, especially its narrow band gap, high refractive index in the visible range, relatively low reflectivity in the visible range, inductive behavior, and strong UV absorption, allow for effective light trapping, making it a good option for solar energy devices.[75,81]

https://doi.org/10.1021/acs.jpcc.4c06553
J. Phys. Chem. C 2025, 129, 2672−2690

Table 4. Calculated Thermoelectric Properties of FeMnScAl Spin-Up (↑)

temperature (°K)	GGA N↑	mBJ N↑	GGA S↑ (eV/K)	MbjS↑ (eV/K)	GGA σ ↑ (1/ΩmsK)	mBJ σ ↑ (1/ΩmsK)	GGA κ_e↑ (W/mK)	mBJ κ_e ↑ (W/mK)
50	−3.01494	−3.01545	2.19×10^5	2.16×10^5	1.08×10^{20}	1.09×10^{20}	8.96×10^{13}	8.33×10^{13}
300	−3.01857	−3.02064	−203.7	−252	8.13×10^{19}	8.16×10^{19}	6.71×10^{14}	6.94×10^{14}
500	−3.03046	−3.03562	−420	−465.15	8.76×10^{19}	8.91×10^{19}	1.51×10^{15}	1.56×10^{15}

Table 5. Calculated Thermoelectric Properties of FeMnScAl Spin-Down (↓)

temperature (°K)	GGA N↓	mBJ N↓	GGAS↓ (eV/K)	mBJS↓ (eV/K)	GGAσ ↓ (1/ΩmsK)	mBJ σ ↓ (1/ΩmsK)	GGA κ_e ↓ (W/mK)	mBJ κ_e ↓ (W/mK)
50	2.9629	2.98436	-1.032×10^{-4}	−0.0001563	1.04422×10^{19}	4.68005×10^{18}	1.63×10^{13}	1.04864×10^{13}
300	2.85302	2.8897	-1.817×10^{-4}	−0.0001957	2.64016×10^{19}	2.1127×10^{19}	4.38×10^{14}	3.86232×10^{14}
500	2.73915	2.78327	-1.515×10^{-4}	−0.0001598	4.30213×10^{19}	3.69149×10^{19}	1.25×10^{15}	1.15416×10^{15}

3.7. Thermoelectric Properties. Thermoelectric materials technology is important for converting waste heat into electricity, which has applications across various industries.[82] This technology depends on the Seebeck and Peltier effects (producing voltage based on temperature difference) in order to generate electricity out of heat or as a cooling medium.[83] A key parameter for evaluating material performance in these applications is the figure of merit (ZT), derived by the formula $\left(\mathrm{ZT} = \frac{S^2\sigma T}{\kappa_e + \kappa_l}\right)$; where S: Seebeck coefficient, σ: electrical conductivity, κ_l: lattice thermal conductivity, and κ_e: electronic contribution to thermal conductivity; PF = S^2 σ is the power factor.[82] High-efficiency thermoelectric materials demand a unique set of properties: a large Seebeck coefficient, excellent electrical conductivity, and minimal heat conduction. However, this optimization process can be difficult due to the fact that increasingly large values of effective mass (m^*) and the carrier concentration (n) are associated with lower values of the Seebeck coefficient (S) and electrical conductivity (σ).[84,85]

The relationship between κ_e and σ defined by the Wiedemann−Franz law introduces challenges in the optimization of thermoelectric materials ($\kappa_e = l\sigma$ T), where (l) is the Lorentz number. A careful balance among these elements is necessary for these materials to display thermoelectric features.[86,87]

This section presents an analysis of the thermoelectric properties of the FeMnScAl alloy in order to determine the relevance of its use as a thermoelectric material. The software of BoltzTraP contains a semiclassical procedure based on the Boltzmann transport theory to evaluate the electronic band structure and thermoelectric properties in the temperature range 50−500 K, around the Fermi level (where $E-EF \approx 0$).[30] The Bolzmann transport equation evaluates important parameters such as the Seebeck coefficient (s), electronic component of thermal conductivity (κ_e), and electrical conductivity (σ). The only exception of unevaluated values is the lattice thermal conductivity (κ_l). To ensure accurate results, a good understanding of the electronic band structure is necessary. To refine the band energies, this method adapts the DFT-derived energies using basic functions such as Fourier series or polynomials to create an analytical model that facilitates transport calculations. This model, based on Boltzmann theory, agrees with experimental data in many systems.[30] For spin-polarized systems, the Seebeck coefficient (S) is expressed as[23,88]

$$S = S(\uparrow)\left\{\frac{1 + \left[\frac{s(\uparrow)}{s(\downarrow)}\right]\left[\frac{\sigma(\downarrow)}{\sigma(\uparrow)}\right]}{1 + \left[\frac{\sigma(\downarrow)}{\sigma(\uparrow)}\right]}\right\} \quad (16)$$

where $S\uparrow$ and $\sigma\uparrow$ are the Seebeck coefficients and electrical conductivities for the spin-up and direction, while $S\downarrow$ and $\sigma\downarrow$ are for the spin-down direction.

Figure 14 presents the temperature-dependent thermoelectric properties of the material, separating the data into spin-up and spin-down channels in the region where $E - E_F = 5.03 \times 10^{-3}$ eV. Figure 14a shows the temperature dependence of the spin-up electronic DOS ($N\uparrow$). As the temperature increases, $N\uparrow$ slightly decreases for both GGA and mBJ. Figure 14b displays the spin-down electronic density ($N\downarrow$) as a function of temperature. The trend is consistent with the spin-up channel, with $N\downarrow$ decreasing as the temperature rises for both methods (mBJ − GGA). The Seebeck coefficient for the spin-up channel ($S\uparrow$) is plotted against the temperature in Figure 14c. $S\uparrow$ decreases with temperature in both GGA and mBJ; positive and negative values of the Seebeck coefficient ($S\uparrow$) indicate that p-type and n-type charge carriers are present in this specified temperature range. Figure 14d presents the Seebeck coefficient for the spin-down channel ($S\downarrow$) as a function of the temperature. The $S\downarrow$ shows a decreasing pattern with increasing temperature up to 200 K, taking a high value of 196 μV K^{-1} at 300 K, followed by a gradual increase as the temperature is raised further up to 500 K. Positive values of the Seebeck coefficient ($S\downarrow$) indicate that p-type charge are the main type of charge carriers within this temperature range. Figure 14e illustrates the temperature-dependent electrical conductivity for the spin-up channel ($\sigma\uparrow$). As the temperature increases, σ decreases, and then increases, with GGA and mBJ showing close agreement at lower temperatures but diverging slightly at higher temperatures. The spin-down electrical conductivity ($\sigma\downarrow$) also varies with the temperature. Both GGA and mBJ show an increasing trend with temperature, as shown in Figure 14f. For two approximation methods (GGA-mBJ), Figure 14g shows the electronic thermal conductivity for the spin-up channel ($\kappa_e\uparrow$) as a function of the temperature. $\kappa_e\uparrow$ increases steadily with the temperature. Furthermore, the spin-down electronic thermal conductivity ($\kappa_e\downarrow$) is plotted in Figure 14h, and like the spin-up channel, $\kappa_e\downarrow$ increases with temperature for GGA and mBJ. Analysis of the FeMnScAl alloy showed variations in electrical conductivity depending on the spin state, with the spin-up channel showing higher conductivity than the spin-down channel near the Fermi level, highlighting its half-metallic behavior. Both spin states show

https://doi.org/10.1021/acs.jpcc.4c06553
J. Phys. Chem. C 2025, 129, 2672−2690

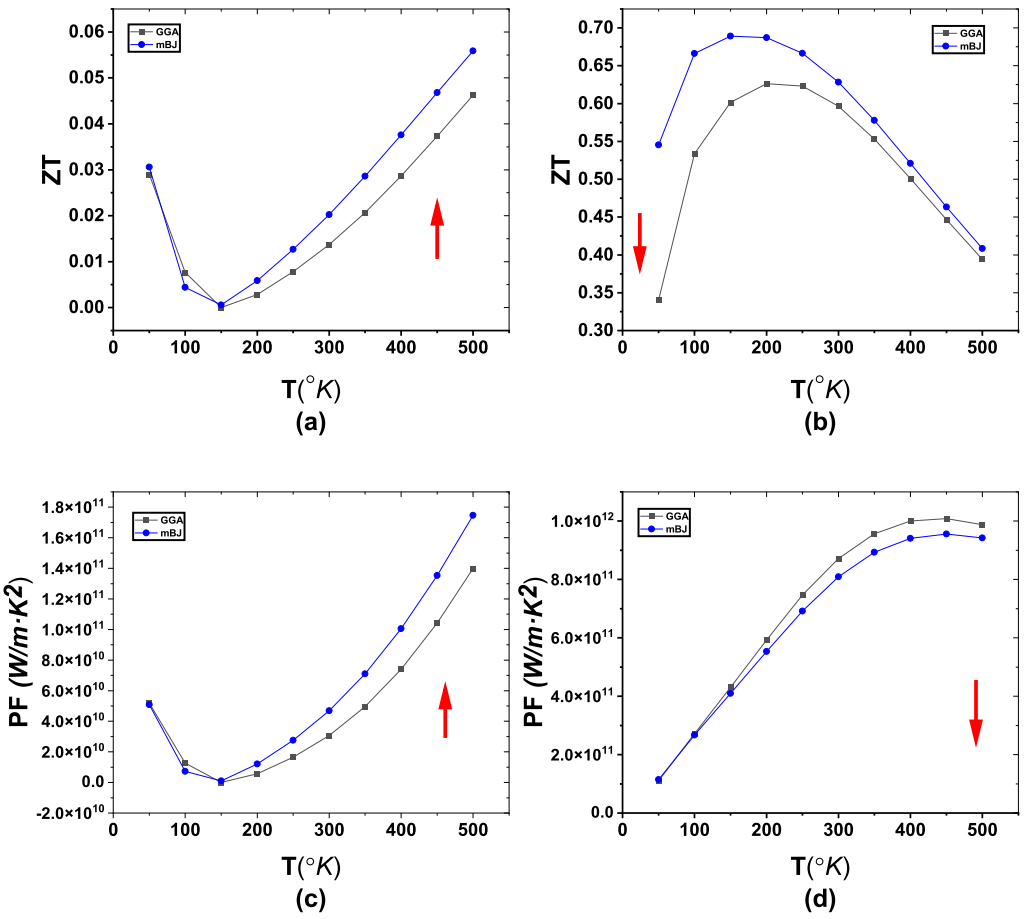

Figure 15. (a–d) Thermoelectric figure of merit (ZT) and power factor (PF) for FeMnScAl alloy.

Table 6. Figure of Merit (ZT) and Power Factor (PF) in (m^3/C) for Specific Temperature Values

<!—Col Count:9(temperature (°K)	GGA *ZT*↑	mbJ *ZT*↑	GGA *ZT*↓	mbJ *ZT*↓	GGA *PF*↑	mbJ *PF*↑	GGA *PF*↓	mbJ *PF*↓
50	0.02897	0.03057	0.34034	0.54548	5.19×10^{10}	5.09×10^{10}	1.11×10^{11}	1.14×10^{11}
300	0.01372	0.02024	0.59639	0.62841	3.07×10^{10}	4.68×10^{10}	8.71×10^{11}	8.09×10^{11}
500	0.04623	0.0559	0.39418	0.40836	1.40×10^{11}	1.75×10^{11}	9.88×10^{11}	9.43×10^{11}

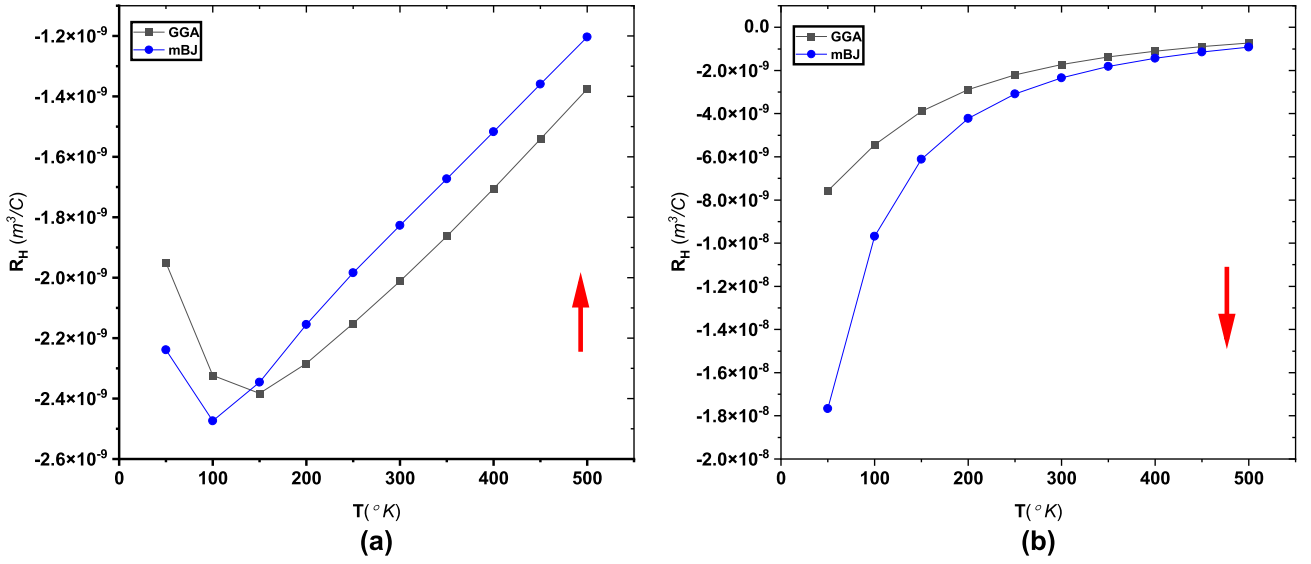

Figure 16. Hall coefficient R_H of the FeMnScAl compound for both spin directions with GGA and mBJ methods.

https://doi.org/10.1021/acs.jpcc.4c06553
J. Phys. Chem. C 2025, 129, 2672−2690

Table 7. Hall Coefficient (R_H) Values for the FeMnScAl Alloy for Specific Temperature Values

	GGA	mBJ	GGA	mBJ
T(°K)	$R_H\uparrow$	$R_H\uparrow$	$R_H\downarrow$	$R_H\downarrow$
50	-1.95×10^{-9}	-2.24×10^{-9}	-7.58×10^{-9}	-1.77×10^{-8}
300	-2.01×10^{-9}	-1.83×10^{-9}	-1.72×10^{-9}	-2.34×10^{-9}
500	-1.38×10^{-9}	-1.20×10^{-9}	-7.29×10^{-9}	-9.20×10^{-10}

increasing electronic conductivity with temperature. The calculated thermoelectric properties of FeMnScAl for the spin-up (↑) and spin-down (↓) channels at specific temperatures are listed in Tables 4 and 5, respectively.

Figure 15 shows the computed thermoelectric figure of merit (ZT) and the power factor (PF). Figure 15a shows that with the rise in temperature, the spin-up figure of merit (ZT↑) initially decreases for the spin-up configuration. It shows a minimum at 100 K and beyond the minimum point; the ZT↑ increases further with the increase in temperature up to 500 K. The calculated value of (ZT↓) for the case of the spin down configuration is shown to increase initially with increasing temperature and reaches its peak value of 0.689 at 150 K for the mBJ approximation. Above this maximum, ZT↓ decreases gradually with a further increase in temperature, as illustrated in Figure 15b.

Figure 15c, for the spin-up state, thePF↑ increases with temperature for both the GGA and mBJ approximations, shows a peak around 400 K before declining slightly. Figure 15d, the spin-down PF↓ first decreases and reaches a minimum at 100 K. Beyond this temperature, the PF↓ rises significantly with an increase in temperature, which indicates greater power generation possibility at higher temperatures for both spin configurations. However, in the case of higher temperature, PF of both spin-up and spin-down configurations shows quite a pattern similar to that of ZT. In this regard, the value of ZT obtained for the FeMnScAl alloy in a spin-down configuration at room temperature (300 K) exhibits quite encouraging features toward thermoelectric performance. Table 6 lists the ZT and PF values for the FeMnScAl alloy across the specified temperature points.

The Hall coefficient (R_H) of the FeMnScAl alloy is negative for both spin-up and spin-down channels across the temperature range shown in Figure 16, indicating electron-dominated conduction. In the spin-up channel, it decreases to a minimum at 100 K for mBJ and 150 K for GGA, and then increases with temperature. While for the spin-down channel, it follows a more pronounced increase that reaches its maximum at 500 K. The presence of negative R_H values for both spin channels along the whole temperature range, indicating that the majority carriers are electrons (n-type).[89] The specific values of R_H are provided in Table 7.

The Slack model, as specified in eq 17, was employed to measure the lattice thermal conductivity (κ_l) in the FeMnScAl alloy[90,91]

$$\kappa_l = A\frac{M_a\theta^3\delta}{\gamma^2 \mathrm{Tn}^{2/3}} \tag{17}$$

In this model, A denotes the Slack constant, which serves as a coefficient in eq 17 and is determined as follows

$$A = \frac{2.43 \times 10^{-8}}{1 - \frac{0.541}{\gamma} - \frac{0.228}{\gamma^2}} \tag{18}$$

The average atomic mass (M_a) is a key factor in determining the material's thermal conductivity. The space occupied by each atom within a unit cell is reflected in the atomic volume, δ, while θ_β represents the Debye temperature. The number of atoms per unit cell is denoted by n and T signifies the absolute temperature. The dimensionless Grüneisen parameter (γ) quantifies how changes in volume affect a lattice's vibrational frequencies[91]

$$\gamma = \frac{9 - 12\left(\frac{V_t}{v_l}\right)^2}{2 - 4\left(\frac{V_t}{v_l}\right)^2} \tag{19}$$

where V_t is the transverse elastic wave velocity and V_l is the longitudinal elastic wave velocity. Computation of the Grüneisen parameter γ and Debye temperature θ_D was performed utilizing the WIEN2k software in combination with its IRelast functionality.[25,26] Figures 17 and 18 illustrate

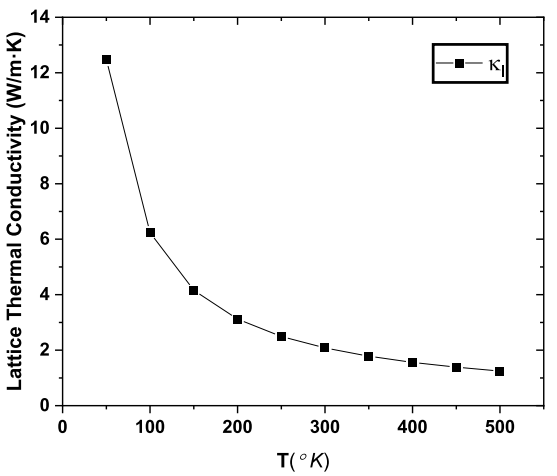

Figure 17. Lattice thermal conductivity vs temperature using the Slack model.

the lattice and total thermal conductivity, respectively, as they vary with the temperature. In Figure 17, the lattice thermal conductivity decreases sharply up to 200 K, maybe because of increased phonon scattering, and then more gradually up to 500 K. The measured value at 300 K is 2.079 W/mK. As shown in Figure 18, the spin-down total conductivity (κ_{tot}), like the electronic thermal conductivity (κ_e), increases with the temperature in both GGA and mBJ calculations, suggesting that the lattice thermal conductivity contribution is relatively minor. The spin-down state was chosen for this analysis because it is particularly important for understanding the electronic transitions.

These results underscore the exceptional promise of the FeMnScAl spin-down channel for thermoelectric applications, particularly when the compound exhibits a semiconducting behavior. This potential is clearly demonstrated by the high

https://doi.org/10.1021/acs.jpcc.4c06553
J. Phys. Chem. C 2025, 129, 2672−2690

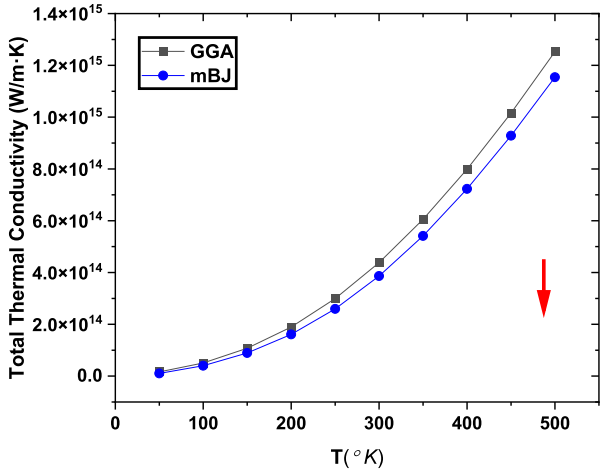

Figure 18. Total thermal conductivity variations with temperature.

Seebeck coefficient (196 μV K^{-1} at 300 K) and the remarkable peak figure of merit (ZT↓) of 0.689 observed at 150 K, exceeding the performance observed in the spin-up channel. These findings highlight the spin-down channel's significant potential for efficient waste heat recovery.[92,93]

4. CONCLUSIONS

In conclusion, the study shows that the Heusler quaternary compound FeMnScAl has great potential for use in spintronics, thermoelectrics, and green energy technologies. DFT analysis reveals the thermodynamic and mechanical stability of FeMnScAl. It also shows half-metallicity and ferromagnetism along with good optical properties for solar energy applications. Moreover, its high Seebeck coefficient and ZT value highlight its ability to work well for efficient, low-cost thermoelectric devices. As summarized in Table 8, the key properties of FeMnScAl, including its stability, half-metallicity, magnetic moment, and optical characteristics, position it as a strong candidate for these applications. These findings are encouraging, but more experiments are needed to completely understand its potential in advanced technology uses.

Table 8. Key Properties of the FeMnScAl Type 2 Heusler Compound

property	value/description
stability	thermodynamically and mechanically stable
lattice parameter	6.1532 Å
electronic character	half-metallic
magnetic property	ferromagnetic
magnetic moment	3.00 μB
band gap	0.1574 eV
refractive index	2.63 < $n(\omega)$ < 3.77 in visible spectrum
optical properties	low reflectivity in visible spectrum, strong UV absorption
thermoelectric figure of merit (ZT)	0.628 (at room temperature)
Seebeck coefficient	196 μV K^{-1} (at room temperature)
potential applications	spintronics, solar energy, and thermoelectric devices

ASSOCIATED CONTENT

Data Availability Statement

The data presented in this study are available upon request from the corresponding author. The data are not publicly available due to privacy concerns.

AUTHOR INFORMATION

Corresponding Author

Mohammed S. Abu-Jafar − *Department of Physics, An-Najah National University, Nablus 00970, Palestine;* orcid.org/0000-0003-1645-4974; Email: mabujafar@najah.edu

Authors

Hasan A. Masri − *Department of Physics, An-Najah National University, Nablus 00970, Palestine*

Abdelmadjid Bouhemadou − *Laboratory for Developing New Materials and Their Characterizations, Department of Physics, Faculty of Science, Ferhat Abbas University - Setif 1, 19000 Setif, Algeria*

Nadjib Baadji − *Département de Physique & Laboratoire de Physique des Matériaux et Ses Applications, Faculté des Sciences, Université Mohamed Boudiaf, M'sila 28000, Algeria*

Complete contact information is available at: https://pubs.acs.org/10.1021/acs.jpcc.4c06553

Author Contributions

Hasan A. Masri: conceptualization, methodology, data curation, software, and writing-original draft preparation. Mohammed S. Abu-Jafar: conceptualization, methodology, data curation, supervision, and writing−reviewing and editing. Abdelmadjid Bouhemadou: data curation (supporting) and software (supporting). Nadjib Baadji: data curation (supporting) and software (supporting).

Funding

This research received no external funding.

Notes

The authors declare no competing financial interest.

ACKNOWLEDGMENTS

I would like to express my great gratitude to Dr. Ahmad Yousef and Eng. Ali Masri for the valuable support during this research. Their assistance and technical abilities were crucial for completing this work. I also would like to thank Eng. Nisreen Hamadneh for her assistance in installing the Wien2K code.

REFERENCES

(1) Palmstrøm, C. J. Heusler compounds and spintronics. *Prog. Cryst. Growth Charact. Mater.* **2016**, *62*, 371−397.

(2) Kamlesh, P. K.; Gautam, R.; Kumari, S.; Verma, A. S. Investigation of inherent properties of XScZ (X = Li, Na, K; Z = C, Si, Ge) half-Heusler compounds: Appropriate for photovoltaic and thermoelectric applications. *Phys. B (Amsterdam, Neth.)* **2021**, *615*, 412536.

(3) Gayner, C.; Kar, K. K. Recent advances in thermoelectric materials. *Prog. Mater. Sci.* **2016**, *83*, 330−382.

(4) Wederni, A.; Daza, J.; Ben Mbarek, W.; Saurina, J.; Escoda, L.; Suñol, J.-J. Crystal Structure and Properties of Heusler Alloys: A Comprehensive Review. *Metals* **2024**, *14*, 688.

(5) Hossain, M. A.; Rahman, Md.T.; Khatun, M.; Haque, E. Structural, elastic, electronic, magnetic and thermoelectric properties of new quaternary Heusler compounds CoZrMn X (X = Al, Ga, Ge, In). *Comput. Condensed Matter* **2018**, *15*, 31−41.

(6) Bouferrache, K.; Ghebouli, M. A.; Slimani, Y.; Ghebouli, B.; Fatmi, M.; Chihi, T.; Algethami, N.; Mouhammad, S. A.; Alomairy, S.; Elkenany, E. B. Structural stability, opto-electronic, magnetic and thermoelectric properties of half-metallic ferromagnets quaternary Heusler alloys CoFeXAs (X = Mn, Cr and V). *Solid State Commun.* **2024**, *377*, 115366.
(7) Xia, Z.; Liu, Z.; Zhang, Q.; Zhang, Y.; Ma, X. Magnetic and anomalous transport properties in spin-gapless semiconductor like quaternary Heusler alloy CoFeTiSn. *J. Magn. Magn. Mater.* **2022**, *553*, 169283.
(8) Wei, X.-P.; Mei, Z.-Y.; Liu, X.; Tao, X. Investigations on stability, Gilbert damping, electronic and magnetic properties along with Curie temperature for quaternary Heusler alloys CrTiCoZ. *Results Phys.* **2024**, *58*, 107512.
(9) Khadhraoui, Z.; Amara, S. E.; Behlali, A. Y.; Kheribot, H.; Makhlouf, S.; Labidi, S.; Amara, A. Comprehensive analysis: Exploring quaternary Heusler alloys CoFeXGe (X = Hf and Ta) through first-principles calculations. *J. Am. Ceram. Soc.* **2024**, *107*, 7421−7440.
(10) Frioui, H.; Meddour, A.; Gous, M. H. Structural, mechanical, electronic, magnetic, optical, and thermoelectric properties of a new equiatomic quaternary heusler compound FeZrCrZ (Z = Si, Ge, Sn): A first-principles investigation. *Mater. Sci. Semicond. Process.* **2024**, *182*, 108697.
(11) Suktel, L.; Saini, S. M. Thermoelectric performance of newly discovered LiHfPdZ (Z= Al, Ga, and In) quaternary Heusler compounds: A DFT study. *Phys. B (Amsterdam, Neth.)* **2024**, *690*, 416268.
(12) Ketfi, M.; Berri, S.; Maouche, D.; Bouarissa, N. Structural, Electronic, Half-Metallic and Thermoelectric Properties of Quaternary Heusler Alloys AgCoFeZ (Z = Al, Ga, Si, Ge, and Sn), NiFeCrZ(Z = Al, Si, Ge, In) and NdCoMnGa: a First Principles Study. *J. Supercond. Novel Magn.* **2024**, *37*, 737−751.
(13) Seh, A. Q.; Gupta, D. C. Quaternary Heusler alloys a future perspective for revolutionizing conventional semiconductor technology. *J. Alloys Compd.* **2021**, *871*, 159560.
(14) Gao, Y. C.; Gao, X. The half-metallicity of LiMgPdSn-type quaternary Heusler alloys FeMnScZ (Z = Al, Ga, In): A first-principle study. *AIP Adv.* **2015**, *5* (5), 057157−057157−10.
(15) Kohn, W.; Sham, L. J. Self-consistent equations including exchange and correlation effects. *Phys. Rev.* **1965**, *140*, A1133.
(16) Blaha, P.; Schwarz, K.; Tran, F.; Laskowski, R.; Madsen, G. K. H.; Marks, L. D. WIEN2k: An APW+lo program for calculating the properties of solids. *J. Chem. Phys.* **2020**, *152*, 074101.
(17) Gutiérrez Moreno, J. J.; Cao, J.; Fronzi, M.; Assadi, M. H. N. A review of recent progress in thermoelectric materials through computational methods. *Mater. Renew. Sustain. Energy* **2020**, *9*, 16.
(18) Blügel, S.; Bihlmayer, G. Full-potential linearized augmented planewave method. In *Computational Nanoscience: Do It Yourself*; John von Neumann Institute for Computing, Forschungszentrum Julich, 2006; Vol. *31*, pp 85−129.NIC Series
(19) Blaha, P.; Schwarz, K.; Sorantin, P.; Trickey, S. B. Full-potential, linearized augmented plane wave programs for crystalline systems. *Comput. Phys. Commun.* **1990**, *59*, 399−415.
(20) Perdew, J. P.; Burke, K.; Ernzerhof, M. Generalized Gradient Approximation Made Simple. *Phys. Rev. Lett.* **1996**, *77*, 3865.
(21) Ernzerhof, M.; Scuseria, G. E. Assessment of the Perdew-Burke-Ernzerhof exchange-correlation functional. *J. Chem. Phys.* **1999**, *110*, 5029−5036.
(22) Camargo-Martínez, J. A.; Baquero, R. Performance of the modified Becke-Johnson potential for semiconductors. *Phys. Rev. B:Condens. Matter Mater. Phys.* **2012**, *86*, 195106.
(23) Bhat, T. M.; Singh, S.; Gupta, D. C. Electronic and Transport Properties of LaNi4Sb12 Skutterudite: Modified Becke-Johnson Approach. *J. Electron. Mater.* **2018**, *47*, 4544−4549.
(24) Tran, F.; Blaha, P. Accurate Band Gaps of Semiconductors and Insulators with a Semilocal Exchange-Correlation Potential. *Phys. Rev. Lett.* **2009**, *102*, 226401.
(25) Golesorkhtabar, R.; Pavone, P.; Spitaler, J.; Puschnig, P.; Draxl, C. ElaStic: A tool for calculating second-order elastic constants from first principles. *Comput. Phys. Commun.* **2013**, *184*, 1861−1873.
(26) Charpin, T. *A package for calculating elastic tensors of cubic phase using WIEN*; Laboratory of Geometrix: Paris, 2001.
(27) Ambrosch-Draxl, C.; Majewski, J. A.; Vogl, P.; Leising, G. First-principles studies of the structural and optical properties of crystalline poly(*para* -phenylene). *Phys. Rev. B* **1995**, *51*, 9668−9676.
(28) Ambrosch-Draxl, C.; Sofo, J. O. Linear optical properties of solids within the full-potential linearized augmented planewave method. *Comput. Phys. Commun.* **2006**, *175*, 1−14.
(29) Rathgen, H.; Katsnelson, M. I. Symmetry Assumptions, Kramers-Kronig Transformation and Analytical Continuation in Ab Initio Calculations of Optical Conductivities. *Phys. Scr.* **2004**, *T109*, 170.
(30) Madsen, G. K. H.; Singh, D. J. BoltzTraP. A code for calculating band-structure dependent quantities. *Comput. Phys. Commun.* **2006**, *175*, 67−71.
(31) Özdoğan, K.; Şaşıoğlu, E.; Galanakis, I. Slater-Pauling behavior in LiMgPdSn-type multifunctional quaternary Heusler materials: Half-metallicity, spin-gapless and magnetic semiconductors. *J. Appl. Phys.* **2013**, *113*, 193903.
(32) Hoat, D. M.; Naseri, M. Examining the half-metallicity and thermoelectric properties of new equiatomic quaternary Heusler compound CoVRhGe under pressure. *Phys. B (Amsterdam, Neth.)* **2020**, *583*, 412058.
(33) Murnaghan, F. D. The Compressibility of Media under Extreme Pressures. *Proc. Natl. Acad. Sci. U.S.A.* **1944**, *30*, 244−247.
(34) Lucia, O.; Maussion, P.; Dede, E. J.; Burdio, J. M. Induction heating technology and its applications: Past developments, current technology, and future challenges. *IEEE Trans. Ind. Electr.* **2014**, *61*, 2509−2520.
(35) Wang, J.; Zhou, Y. Dependence of elastic stiffness on electronic band structure of nanolaminate M2A1C (M = Ti,V,Nb, and Cr) ceramics. *Phys. Rev. B:Condens. Matter Mater. Phys.* **2004**, *69*, 214111.
(36) Zada, Z.; Ullah, H.; Bibi, R.; Zada, S.; Mahmood, A. Electronic band profiles and magneto-electronic properties of ternary XCu2P2(X = Ca, Sr) compounds: Insight from ab initio calculations. *Z. Naturforsch.* **2020**, *75*, 543−549.
(37) Gunnarsson, O.; Andersen, O. K.; Jepsen, O.; Zaanen, J. Density-functional calculation of the parameters in the Anderson model: Application to Mn in CdTe. *Phys. Rev. B* **1989**, *39*, 1708.
(38) Azar, S. M.; Mousa, A. A.; Khalifeh, J. M. Structural, electronic and magnetic properties of Ti1+xFeSb Heusler alloys. *Intermetallics* **2017**, *85*, 197−205.
(39) Segall, M. D.; Lindan, P. J. D.; Probert, M. J.; Pickard, C. J.; Hasnip, P. J.; Clark, S. J.; Payne, M. C. First-principles simulation: ideas, illustrations and the CASTEP code. *J. Phys.: Condens. Matter* **2002**, *14*, 2717−2744.
(40) Suetin, D. V.; Shein, I. R. Electronic Structure, Mechanical and Dynamical Stability of Hexagonal Subcarbides M2C (M = Tc, Ru, Rh, Pd, Re, Os, Ir, and Pt): Ab Initio Calculations. *Phys. Solid State* **2018**, *60*, 213−224.
(41) Khandy, S. A.; Chai, J.-D. Novel half-metallic L21 structured full-Heusler compound for promising spintronic applications: A DFT-based computer simulation. *J. Magn. Magn. Mater.* **2019**, *487*, 165289.
(42) Khandy, S. A. Inspecting the electronic structure and thermoelectric power factor of novel p-type half-Heuslers. *Sci. Rep.* **2021**, *11*, 20756.
(43) Khandy, S. A.; Chai, J.-D. Strain engineering of electronic structure, phonon, and thermoelectric properties of p-type half-Heusler semiconductor. *J. Alloys Compd.* **2021**, *850*, 156615.
(44) Khandy, S. A.; Chai, J.-D. Origin of pseudo gap and thermoelectric signatures of semimetallic Ru2TaGa: Structural stability from phonon dynamics, mechanical, and thermodynamic predictions. *J. Phys. Chem. Solids* **2021**, *154*, 110098.
(45) Reshak, A. H.; Alahmed, Z. A.; Azam, S. Electronic Structure, Electronic Charge Density and Optical Properties Analyses of

https://doi.org/10.1021/acs.jpcc.4c06553
J. Phys. Chem. C 2025, 129, 2672−2690

Rb2Al2B2O7 Compound: DFT Calculation. *Int. J. Electrochem. Sci.* **2014**, *9*, 975−989.
(46) Abraham, J. A.; Pagare, G.; Sanyal, S. P. Electronic Structure, Electronic Charge Density, and Optical Properties Analysis of GdX_3 (X = In, Sn, Tl, and Pb) Compounds: DFT Calculations. *Indian J. Mater. Sci.* **2015**, *2015*, 1−11.
(47) Graf, T.; Felser, C.; Parkin, S. S. P. Simple rules for the understanding of Heusler compounds. *Prog. Solid State Chem.* **2011**, *39*, 1−50.
(48) Reuss, A. Berechnung der Fließgrenze von Mischkristallen auf Grund der Plastizitätsbedingung für Einkristalle. *J. Appl. Math. Mech.* **1929**, *9*, 49−58.
(49) Born, M.; Huang, K. *Dynamical Theory Of Crystal Lattices*; Oxford University Press New York: NY, 1996; ..
(50) Zener, C. M.; Siegel, S. Elasticity and Anelasticity of Metals. *J. Phys. Colloid Chem.* **1949**, *53*, 1468.
(51) Pugh, S. F. XCII. Relations between the elastic moduli and the plastic properties of polycrystalline pure metals. *London, Edinburgh Dublin Phil. Mag. J. Sci.* **1954**, *45*, 823−843.
(52) Greaves, G. N.; Greer, A. L.; Lakes, R. S.; Rouxel, T. Poisson's ratio and modern materials. *Nat. Mater.* **2011**, *10*, 823−837.
(53) Frantsevich, I. N.; Voronov, F. F.; Bokuta, S. A. *Elastic Constants and Elastic Moduli of Metals and Insulators Handbook*; Naukova Dumka: Kyiv, Ukraine, 1983; pp 60−180.
(54) Soh, J. W.; Lee, H. M.; Kwon, H. S. Relation between Poisson's ratio and ionicity in simple binary cubic compounds. *J. Alloys Compd.* **1993**, *194*, 119−125.
(55) Ravindran, P.; Fast, L.; Korzhavyi, P. A.; Johansson, B.; Wills, J.; Eriksson, O. Density functional theory for calculation of elastic properties of orthorhombic crystals: Application to TiSi2. *J. Appl. Phys.* **1998**, *84*, 4891−4904.
(56) Wortmann, D.; Michalicek, G.; Baadji, N.; Beida, W.; Betzinger, M.; Bihlmayer, G.; Bornhake, T.; Bröder, J., Burnus, T.; Enkovaara, J., et al., *Fleur*, Zenodo,(2023).
(57) Wang, D.; Wu, R.; Freeman, A. J. First-principles theory of surface magnetocrystalline anisotropy and the diatomic-pair model. *Phys. Rev. B* **1993**, *47*, 14932−14947.
(58) Skomski, R.; Coey, J. M. D. Magnetic anisotropy - How much is enough for a permanent magnet? *Scr. Mater.* **2016**, *112*, 3−8.
(59) Dewhurst, K.; Sharma, S., ELK code development, (n.d.). https://www2.mpi-halle.mpg.de/theory_department/research/elk_code_development/(accessed April 4, 2024).
(60) Lantri, T.; Bentata, S.; Bouadjemi, B.; Benstaali, W.; Bouhafs, B.; Abbad, A.; Zitouni, A. Effect of Coulomb interactions and Hartree-Fock exchange on structural, elastic, optoelectronic and magnetic properties of Co2MnSi Heusler: A comparative study. *J. Magn. Magn. Mater.* **2016**, *419*, 74−83.
(61) Sharma, S.; Verma, A. S.; Jindal, V. K. Ab initio studies of structural, electronic, optical, elastic and thermal properties of silver gallium dichalcogenides (AgGaX2: X = S, Se, Te). *Mater. Res. Bull.* **2014**, *53*, 218−233.
(62) Kuzmenko, A. B. Kramers-Kronig constrained variational analysis of optical spectra. *Rev. Sci. Instrum.* **2005**, *76*, 083108.
(63) Dresselhaus, M. S. Solid State Physics Optical Properties of Solids; Srisathya Sai College Digital Library, 2022; pp 8−50.
(64) Bakhshayeshi, A.; Sarmazdeh, M. M.; Mendi, R. T.; Boochani, A. First-Principles Prediction of Electronic, Magnetic, and Optical Properties of Co2MnAs Full-Heusler Half-Metallic Compound. *J. Electron. Mater.* **2017**, *46*, 2196−2204.
(65) Jain, V. K.; Lakshmi, N.; Jain, R.; Chandra, A. R. Electronic Structure, Elastic, Magnetic, and Optical Properties of Fe2MnZ (Z = Si, Ge, and Sn) Full Heusler Alloys: First-Principle Calculations. *J. Supercond. Novel Magn.* **2019**, *32*, 739−749.
(66) Khan, S. A.; Reshak, A. H.; Alahmed, Z. A. Electronic band structure and optoelectronic properties of SrCu2X2 (X = As, Sb): DFT calculation. *J. Mater. Sci.* **2014**, *49*, 5208−5217.
(67) Han, D.-A.; Zeng, Y.-G.; Chen, W.-C.; Dong, S.-G.; Huang, C.-Q.; Zhu, C.-Y.; Liang, P.-Y. Sub- and Super-Luminal Phenomena in a Doubly Driven Four-Level System. *Commun. Theory Phys.* **2011**, *55*, 671−675.
(68) Solli, D.; Chiao, R. Y.; Hickmann, J. M. Superluminal effects and negative group delays in electronics, and their applications. *Phys. Rev. E:Stat. Nonlinear Soft Matter Phys.* **2002**, *66*, 4.
(69) Wooten, F. Optical Properties of Solids; Elsevier, 1972; ..
(70) Bennacer, H.; Berrah, S.; Boukortt, A.; Ziane, M. I. Electronic and optical properties of GaInX2 (X = As, P) from first principles study. *Indian J. Pure Appl. Phys.* **2015**, *53*, 181−189.
(71) Kandpal, H. C.; Fecher, G. H.; Felser, C. Calculated electronic and magnetic properties of the half-metallic, transition metal based Heusler compounds. *J. Phys. D Appl. Phys.* **2007**, *40*, 1507.
(72) Idrissi, S.; Jabar, A.; Bahmad, L. A DFT study of the CaMg2As2 material for photovoltaic applications. *Solid State Commun.* **2024**, *392*, 115655.
(73) Oluyamo, S. S.; Agunbiade, D. B. Spin Coated Tin Oxide Thin Film For Optical And Optoelectronic Material Applications. *Int. J. Innov. Res. Adv. Studies* **2016**, *3*, 394−398.
(74) Saeed, N. M. Structural and optical properties of ZnS thin films prepared by spray pyrolysis technique. *J. Al-Nahrain Univ.* **2011**, *14*, 86.
(75) Baker, I. M. II-VI Narrow Bandgap Semiconductors: Optoelectronics. In *Springer Handbook of Electronic and Photonic Materials*, 2017; p 1..
(76) Awais, M.; Hussain, F.; Riaz, K. N.; Niaz, N. A.; Shakoor, A.; Dorigo, T.; Ahmad, F.; Mamtaz, U. First-principles calculations to investigate structural, electronic, and optical properties of AgWO4 and PdWO4 tungstate materials for optoelectronic applications. *Next Mater.* **2024**, *4*, 100113.
(77) Olmon, R. L.; Slovick, B.; Johnson, T. W.; Shelton, D.; Oh, S. H.; Boreman, G. D.; Raschke, M. B. Optical dielectric function of gold. *Phys. Rev. B:Condens. Matter Mater. Phys.* **2012**, *86*, 235147.
(78) Ramanna, J.; Yedukondalu, N.; Ramesh Babu, K.; Vaitheeswaran, G. Ab initio study of electronic structure, elastic and optical properties of anti-perovskite type alkali metal oxyhalides. *Solid State Sci.* **2013**, *20*, 120−126.
(79) Liu, H. L.; Quijada, M.; Romero, D. B.; Tanner, D. B.; Zibold, A.; Carr, G. L.; Berger, H.; Forró, L.; Mihaly, L.; Cao, G.; et al. Drude behavior in the far-infrared conductivity of cuprate superconductors. *Ann. Phys.* **2006**, *518*, 606−618.
(80) Fox, M. Optical properties of solids; Oxford University Press, 2010.
(81) Soussi, A.; Ait Hssi, A.; Boujnah, M.; Boulkadat, L.; Abouabassi, K.; Asbayou, A.; Elfanaoui, A.; Markazi, R.; Ihlal, A.; Bouabid, K. Electronic and Optical Properties of TiO2 Thin Films: Combined Experimental and Theoretical Study. *J. Electron. Mater.* **2021**, *50*, 4497−4510.
(82) Riffat, S. B.; Ma, X. Thermoelectrics: a review of present and potential applications. *Appl. Therm. Eng.* **2003**, *23*, 913−935.
(83) Bhat, T. M.; Gupta, D. C. Robust thermoelectric performance and high spin polarisation in CoMnTiAl and FeMnTiAl compounds. *RSC Adv.* **2016**, *6*, 80302−80309.
(84) Han, M.-K.; Hoang, K.; Kong, H.; Pcionek, R.; Uher, C.; Paraskevopoulos, K. M.; Mahanti, S. D.; Kanatzidis, M. G. Substitution of Bi for Sb and its Role in the Thermoelectric Properties and Nanostructuring in Ag1−xPb18MTe20 (M = Bi, Sb) (x = 0, 0.14, 0.3). *Chem. Mater.* **2008**, *20*, 3512−3520.
(85) Alqurashi, H.; Haleoot, R.; Pandit, A.; Hamad, B. Investigations of the electronic, dynamical, and thermoelectric properties of Cd1-xZnxO alloys: First-principles calculations. *Mater. Today Commun.* **2021**, *28*, 102511.
(86) Bejan, A.; Kraus, A. D. Heat transfer handbook; John Wiley & Sons, 2003.
(87) Singh, S.; Maurya, R. K.; Pandey, S. K. Investigation of thermoelectric properties of ZnV2O4 compound at high temperatures. *J. Phys. D Appl. Phys.* **2016**, *49*, 425601.
(88) Xiang, H. J.; Singh, D. J. Suppression of thermopower of Na*x*CoO2 by an external magnetic field: Boltzmann transport

https://doi.org/10.1021/acs.jpcc.4c06553
J. Phys. Chem. C 2025, 129, 2672−2690

combined with spin-polarized density functional theory. *Phys. Rev. B* **2007**, *76*, 195111.
(89) Salvador, J. R.; Shi, X.; Yang, J.; Wang, H. Synthesis and transport properties of M3Ni3Sb4(M = Zrand Hf): An intermetallic semiconductor. *Phys. Rev. B* **2008**, *77*, 235217.
(90) Morelli, D. T.; Slack, G. A., High Lattice Thermal Conductivity Solids, In *High Thermal Conductivity Materials*; Springer-Verlag, New York, 2006, pp 37−68. .
(91) Hariharan, M.; D, E. R. Investigations on the electronic, optical, thermoelectric and thermodynamic properties of quaternary coinage metal HgSeBr: a DFT study. *Phys. Scr.* **2024**, *99*, 035937.
(92) Lu, X.; Morelli, D. T.; Xia, Y.; Zhou, F.; Ozolins, V.; Chi, H.; Zhou, X.; Uher, C. High Performance Thermoelectricity in Earth-Abundant Compounds Based on Natural Mineral Tetrahedrites. *Adv. Energy Mater.* **2013**, *3*, 342−348.
(93) Haque, E.; Hossain, M. A. Electronic, phonon transport and thermoelectric properties of Cs2InAgCl6 from first-principles study. *Comput. Condensed Matter* **2019**, *19*, No. e00374.

https://doi.org/10.1021/acs.jpcc.4c06553
J. Phys. Chem. C 2025, 129, 2672−2690